



HAL
open science

Stability analysis of natural convective flows in horizontal annuli: effects of axial and radial aspect ratios

G. Petrone, Eric Chénier, Guy Lauriat

► To cite this version:

G. Petrone, Eric Chénier, Guy Lauriat. Stability analysis of natural convective flows in horizontal annuli: effects of axial and radial aspect ratios. *Physics of Fluids*, 2006, 18 (10), pp.104107-1/14. hal-00749542

HAL Id: hal-00749542

<https://hal.science/hal-00749542v1>

Submitted on 3 Jun 2017

HAL is a multi-disciplinary open access archive for the deposit and dissemination of scientific research documents, whether they are published or not. The documents may come from teaching and research institutions in France or abroad, or from public or private research centers.

L'archive ouverte pluridisciplinaire **HAL**, est destinée au dépôt et à la diffusion de documents scientifiques de niveau recherche, publiés ou non, émanant des établissements d'enseignement et de recherche français ou étrangers, des laboratoires publics ou privés.

STABILITY ANALYSIS OF NATURAL CONVECTIVE FLOWS IN HORIZONTAL ANNULI: EFFECTS OF THE AXIAL AND RADIAL ASPECT RATIOS

Giuseppe Petrone,^{*} Eric Chénier,[†] and Guy Lauriat

*Université de Marne la Vallée, Cité Descartes,
Champs-sur-Marne, 77454 MARNE LA VALLEE cedex 2, France*

(Dated:)

Abstract

Linear stability analyses for two-dimensional natural convection in horizontal air-filled annuli are performed for three-dimensional perturbations and radius ratios in the range $1.2 \leq R \leq 3$. Flow transitions from moderate to large gap annuli, which have not been reported before, are thoroughly investigated. As a result, stability diagrams are obtained for finite and for infinite length annuli. The leading disturbances and threshold values are found to agree well with experimental data and three-dimensional numerical solutions. Three-dimensional simulations were also carried out to examine the influence on the flow stability of no-slip boundary conditions at the end walls.

PACS numbers: 44.25.+f Natural convection, 47.20.Bp Buoyancy-driven instabilities, 47.55.Iv Core-annular flows

I. INTRODUCTION

Free convective flow of air in horizontal annuli bounded by two cylinders held at different temperatures has been intensely studied in the last past decades as well experimentally as theoretically and numerically. It is established that the basic flow at small Rayleigh numbers, Ra , consists of two large cells, symmetrically located with respect to the vertical plane containing the cylinder axis. When increasing Ra , this flow becomes unstable and leads to different patterns according to the value of the radius ratio, R .

Extensive numerical simulations for the two-dimensional model of flows in transversal sections of annular spaces were conducted. Under the 2D assumption, dual steady solutions were highlighted when the Rayleigh number exceeds a critical value: one being the crescent-shaped eddy flow commonly observed and the other flow consisting of two counter-rotating eddies and their mirror images¹. The appearance of dual solutions is due to an imperfect trans-critical bifurcation². When the radius ratio tends to 1, the imperfect bifurcation gets closer to the classical pitchfork bifurcation of the Rayleigh-Bénard convection between to infinite parallel plates, with a threshold value $Ra_c = 1708$. A recent 2D stability analysis showed that dual but also triple solutions are indeed stable for certain (Ra, R) -gaps³. Moreover, the flows consisting of two or three counter-rotating eddies and their mirror images are linearly unstable for $R > 2$ (and $Ra < 10,000$) due to the onset of a disturbance breaking the vertical reflection symmetry of the basic flow. Thus, only the common couple of counter-rotating cells remains stable for large radius ratios.

The multi-cellular flow patterns obtained with the 2D-flow model and made of longitudinal rolls confined in the top region of the annular space were observed in experiments for a narrow gap annulus ($R = 1.15$)⁴. These patterns were also shown in three-dimensional numerical simulations in combination with transverse rolls in the upper region of the annulus ($R < 1.2$)⁵. For moderate radius ratios, a three-dimensional spiral motion occurs. It consists of the basic crescent-shaped flow with transverse convective cells at the top of the annular space. This spiral flow was obtained as well in numerical works⁶⁻⁸ as in experiments⁹⁻¹¹. For wide gap annuli, an unsteady régime was experimentally observed by Bishop and Carley¹² ($R = 3.69$) and Labonia *et al.*¹³ ($R = 2.38$). This non steady flow behavior was recently confirmed by 3D-numerical simulations for $R = 2.4$: the thermal plume oscillated in the

each of the transversal section of the annulus¹⁴.

A large number of experimental results for narrow ($R \leq 1.23$), moderate ($1.23 \leq R \leq 1.71$) and wide gap annuli ($R \geq 1.71$) had been put together by Powe *et al.*¹⁰ in order to draw a stability chart showing the critical Grashof number as a function of the modified radius ratio $\sigma = 2/(R - 1)$. This chart clearly depicts the regions where 2D multi-cellular, 3D-spiral and 2D-oscillatory flows respectively occur. An analytical stability analysis of 2D-flows with respect to 3D-disturbances in annuli of infinite length was performed by Mojtabi and Caltagirone^{15,16} for infinitesimal ($1 \leq R \leq 4$) and finite amplitude ($1 \leq R \leq 2$) perturbations. The basic flow was approximated in the vertical upper section of the annulus and the disturbances considered as axisymmetric. For $R = 1$ (i.e. parallel plate limit), the stability thresholds evaluated either by linear stability analysis or by an energetic method are equal to $Ra_c = 1708$. These thresholds augment and diverge from each other when increasing the radius ratio. The linear stability analysis was later on improved by taking into account the azimuthal direction⁶ and, as foreseen, the most unstable disturbance was found to occur in the upper part of the annulus. A numerical three-dimensional linear stability analysis of the crescent-shaped flows was carried-out by Choi and Kim¹⁷ for infinite length annuli and $1.2 \leq R \leq 2$. They demonstrated a weak dependence of the Ra -threshold ($1714 \leq Ra_c \leq 2514$) with the radius ratio ($1.2 \leq R \leq 1.9$). The onset of this instability is due to the growing of transverse rolls at the top of the annulus what qualitatively corresponds to numerical and experimental observations⁶⁻¹¹. For $R = 2$, no critical value was detected for $Ra \leq 100,000$. This lack of a threshold value was attributed to its sharp increase with R .

The main purpose of this paper is to improve the knowledge of the stability thresholds as a function of the radius ratio, for air-filled horizontal annuli. A particular attention will be paid on the sudden disappearance beyond $R = 2$ of the transition due to the onset of transverse rolls as described by Choi and Kim¹⁷. To this end, a three-dimensional linear stability analysis was carried-out for two-dimensional basic flows with $1.2 \leq R \leq 3$ and $Pr = 0.7$. The first part of the present paper describes briefly the numerical methods whereas the results are discussed in the second part, divided into six sections. The basic solutions, which are used to perform the linear stability analyses, are first defined. Afterward, neutral stability curves are described as a function of the wavenumber of the disturbances.

Stability diagrams are then established for annuli of finite length, and the effect of no-slip boundary conditions are studied by performing three-dimensional non-linear simulations. Next, the transitions for infinite length annuli with various radius ratios are investigated. To end, comparisons with numerical and experimental studies are performed and discussed.

II. NUMERICAL METHODS

A. Mathematical model and numerical method

1. Linear and non-linear equations

The air-filled annulus of length L is formed by two coaxial and horizontal cylinders of radii r_i^* and $r_o^* = Rr_i^*$, held at temperatures $T^*(r_i^*) = T_i^*$ and $T^*(r_o^*) = T_o^* < T_i^*$ as illustrated in Fig. 1. Lengths and velocity are scaled by the annulus gap $d = r_o^* - r_i^*$ and the thermal diffusivity velocity α/d , respectively, where α is the thermal diffusivity. The dimensionless temperature is defined by $T = (T^* - T_{ref}^*)/(T_i^* - T_o^*)$ where $T_{ref}^* = (T_i^* + T_o^*)/2$. The dimensionless Navier-Stokes and energy equations, expressed in the Boussinesq approximation, write:

$$\begin{cases} \frac{\partial \vec{u}}{\partial t} = -\vec{\nabla} \cdot (\vec{u} \otimes \vec{u}) + Pr \nabla^2 \vec{u} - \vec{\nabla} p + Ra Pr T \vec{k} \\ \vec{\nabla} \cdot \vec{u} = 0 \\ \frac{\partial T}{\partial t} = -\vec{\nabla} \cdot (\vec{u} T) + \nabla^2 T \end{cases} \quad (1)$$

where $Ra = (g\beta(T_i^* - T_o^*)d^3)/(\nu\alpha)$ and $Pr = \nu/\alpha$ are the Rayleigh and Prandtl numbers with β the thermal expansion coefficient and ν the kinematic viscosity.

The equations are treated in the cylindrical coordinates (r, θ, z) in the domain $0 \leq r \leq 1$, $0 \leq \theta \leq 2\pi$, $0 \leq z \leq A$, where $r = (r^* - r_i^*)/d$ and $A = L/d$ is the axial aspect ratio. No-slip boundary conditions are imposed on the heated inner cylinder ($T_i = 0.5$) and cooled outer cylinder ($T_o = -0.5$).

Consider the two-dimensional steady velocity $\vec{u}_0 = u_0 \vec{e}_r + v_0 \vec{e}_\theta$, temperature T_0 , and pressure p_0 fields and the following three-dimensional disturbances $\delta \vec{u} = \delta u \vec{e}_r + \delta v \vec{e}_\theta + \delta w \vec{e}_z$,

δT and δp satisfying slip boundary conditions on the adiabatic end-walls at $z = 0, A$:

$$\begin{cases} \delta u = \bar{u}(r, \theta, t) \cos(kz) \\ \delta v = \bar{v}(r, \theta, t) \cos(kz) \\ \delta w = \bar{w}(r, \theta, t) \sin(kz) \\ \delta p = \bar{p}(r, \theta, t) \cos(kz) \\ \delta T = \bar{T}(r, \theta, t) \cos(kz) \end{cases} \quad (2)$$

where $k = n\pi/A$ is the dimensionless wavenumber and n is an integer. By substituting in the governing equations (1) the velocity, pressure and temperature fields by $\vec{u}_0 + \delta\vec{u}$, $p_0 + \delta p$ and $T_0 + \delta T$ and by neglecting the second-order transport terms, the variables \bar{u} , \bar{v} , \bar{w} , \bar{p} and \bar{T} satisfy the time-dependent equations:

$$\frac{\partial(f\bar{u})}{\partial r} + \eta \frac{\partial\bar{v}}{\partial\theta} + f k\bar{w} = 0 \quad (3a)$$

$$\begin{aligned} \frac{\partial(f\bar{u})}{\partial t} = & -\frac{\partial(f\bar{u}u_0)}{\partial r} - \frac{\partial(\eta\bar{v}u_0)}{\partial\theta} - f k\bar{w}u_0 + \eta\bar{v}v_0 - \frac{\partial(fu_0\bar{u})}{\partial r} - \frac{\partial(\eta v_0\bar{u})}{\partial\theta} + \eta v_0\bar{v} \\ & - f \frac{\partial\bar{p}}{\partial r} + Pr \left(\frac{\partial}{\partial r} \left[f \frac{\partial\bar{u}}{\partial r} \right] + \frac{\partial}{\partial\theta} \left[\frac{\eta^2}{f} \frac{\partial\bar{u}}{\partial\theta} \right] - f k^2\bar{u} - \frac{2\eta^2}{f} \frac{\partial\bar{v}}{\partial\theta} - \frac{\eta^2\bar{u}}{f} \right) \\ & - RaPr f\bar{T} \cos\theta \end{aligned} \quad (3b)$$

$$\begin{aligned} \frac{\partial(f\bar{v})}{\partial t} = & -\frac{\partial(f\bar{u}v_0)}{\partial r} - \frac{\partial(\eta\bar{v}v_0)}{\partial\theta} - f k\bar{w}v_0 - \eta\bar{u}v_0 - \frac{\partial(fu_0\bar{v})}{\partial r} - \frac{\partial(\eta v_0\bar{v})}{\partial\theta} - \eta u_0\bar{v} \\ & - f \frac{\partial\bar{p}}{\partial\theta} + Pr \left(\frac{\partial}{\partial r} \left[f \frac{\partial\bar{v}}{\partial r} \right] + \frac{\partial}{\partial\theta} \left[\frac{\eta^2}{f} \frac{\partial\bar{v}}{\partial\theta} \right] - f k^2\bar{v} + \frac{2\eta^2}{f} \frac{\partial\bar{u}}{\partial\theta} - \frac{\eta^2\bar{v}}{f} \right) \\ & + RaPr f\bar{T} \sin\theta \end{aligned} \quad (3c)$$

$$\frac{\partial(f\bar{w})}{\partial t} = -\frac{\partial(fu_0\bar{w})}{\partial r} - \frac{\partial(\eta v_0\bar{w})}{\partial\theta} + f k\bar{p} + Pr \left(\frac{\partial}{\partial r} \left[f \frac{\partial\bar{w}}{\partial r} \right] + \frac{\partial}{\partial\theta} \left[\frac{\eta^2}{f} \frac{\partial\bar{w}}{\partial\theta} \right] - f k^2\bar{w} \right) \quad (3d)$$

$$\begin{aligned} \frac{\partial(f\bar{T})}{\partial t} = & -\frac{\partial(f\bar{u}T_0)}{\partial r} - \frac{\partial(\eta\bar{v}T_0)}{\partial\theta} - f k\bar{w}T_0 - \frac{\partial(fu_0\bar{T})}{\partial r} - \frac{\partial(\eta v_0\bar{T})}{\partial\theta} \\ & + \frac{\partial}{\partial r} \left[f \frac{\partial\bar{T}}{\partial r} \right] + \frac{\partial}{\partial\theta} \left[\frac{\eta^2}{f} \frac{\partial\bar{T}}{\partial\theta} \right] - f k^2\bar{T} \end{aligned} \quad (3e)$$

with $\eta = R - 1$ and $f = \eta r + 1$. The boundary conditions for the unknowns \bar{u} , \bar{v} , \bar{w} and \bar{T} are homogeneous.

2. Discretization and solvers

The equations were discretized on a structured and staggered grid by a finite volume method. All spatial derivatives were approximated by a second-order centered scheme. The mesh $[r_i, r_{i+1}] \times [\theta_j, \theta_{j+1}]$ is defined by

$$r_i = \frac{\tanh\left(c_r \left(2^{\frac{i-1}{N_r}} - 1\right)\right) + \tanh(c_r)}{2 \tanh(c_r)}, \quad i = 1, N_r + 1$$

$$\theta_j = \begin{cases} \pi \frac{\exp\left(2\pi c_\theta \frac{j-1}{N_\theta}\right) - 1}{\exp(\pi c_\theta) - 1}, & j = 1, \frac{N_\theta}{2} + 1 \\ 2\pi - \theta_{N_\theta+2-j}, & j = \frac{N_\theta}{2} + 1, N_\theta + 1 \end{cases}$$

where N_r is any integer and N_θ an even integer. To adjust the grid distribution at the upper part of the annulus (near $\theta = \pi$) and in the wall regions, two strictly negative real parameters c_r and c_θ were introduced. If one of these two parameters was zero, the grid distribution was set uniform in the corresponding direction.

The computations of the 2D steady states (\vec{u}_0, T_0, p_0) and of the leading perturbations were already described in details for two-dimensional disturbances³. Briefly, the numerical procedure is as follows: first, the basic solution is obtained by solving the 2D equations (1) at the steady state with the Newton algorithm; the dominant disturbances, solutions of equations (3a-3e), their growth rates λ and frequencies ν_f are then evaluated by the Arnoldi method with a first-order time differencing.

For a given wavenumber, the critical parameter $Ra_c(k)$, which corresponds to a growth rate $\lambda = 0$, is computed iteratively by solving the implicit non-linear equation $\lambda(Ra_c) = 0$ with the Lagrange algorithm. This method simply consists in successive approximations of the threshold value by linear interpolations of the Rayleigh number as a function of the growth rates⁸.

Three-dimensional computations are also performed for finite length annuli with dimensionless length $A = L/d$ and by applying no-slip boundary conditions at the adiabatic end-walls. These simulations were conducted for half-annuli with symmetry conditions in the azimuthal direction at $\theta = 0$ and $\theta = \pi$. The three-dimensional scheme was thoroughly described in a previous paper⁸.

B. Influence of the discretization parameters on $Ra_c(k)$

The validity of the numerical results was checked in a previous paper³ for 2D-disturbances ($k = 0$): the relative differences between our threshold values for the saddle-node bifurcation and the critical values published by Mizushima *et al.*² are less than 0.25% for $1.2 \leq R \leq 3$. A good agreement is also shown with the Choi and Kim's results¹⁷ for 3D-disturbances: in infinite length annuli and $R < 2$, the critical Rayleigh numbers and wavenumbers differ from less than 1.5 % and 1 % respectively. In order to better underline the agreements and explain the few observed disagreements between our results and the 3D-linear stability results of the archival literature, the detailed comparisons are deferred for the Results section III E.

To ensure the convergence of solutions, numerous checks were also conducted to measure the sensitivity of the growth rate λ and frequency ν_f of the dominant perturbation as well as the dependency of the critical Rayleigh number as a function of the time step and mesh size. In the next paragraphs, the radius ratio, wavenumber and Rayleigh number values are chosen to be representative of each of the transitions discussed in the Results section. Tests were performed for $(R, k) = (1.2, 3)$ and $1700 \leq Ra \leq 1800$, for $(R, k) = (2.6, 5)$ and $124,500 \leq Ra \leq 129,500$, for $(R, k) = (1.6, 4.5)$ and $10,000 \leq Ra \leq 10,250$ and for $(R, k) = (1.6, 3.2)$ and $19,000 \leq Ra \leq 19,500$.

1. Temporal accuracy

The growth rates λ were evaluated by the Arnoldi method based on a first-order time differencing³ of the linearized Navier-Stokes and energy equations (Eq. 3). Let Δt the time step of the temporal scheme. For each set of R , Ra and k and for the 60×240 mesh, the points $(\Delta t, \lambda)$ are basically aligned along a straight line. This result assess the order of the time approximation. The reference growth rate, λ_{ref} , is thus defined as the extrapolated value corresponding to $\Delta t = 0$.

Tables Ia-Ic illustrate the convergence of λ as a function of the time step for three sets of radius ratio, wavenumber and Rayleigh number. For $\Delta t = 5 \cdot 10^{-5}$, the relative discrepancies with λ_{ref} are systematically less than 0.5%. For $R = 1.6$, $k = 3.2$, $Ra = 19,000$ and $Ra = 19,500$ the dominant perturbation is oscillatory with a frequency ν_f . As shown in Tab. II, the growth rates are not properly evaluated whereas the frequencies are weakly

affected by Δt . For the smallest time step ($\Delta t = 5 \cdot 10^{-6}$), the relative difference between λ and λ_{ref} is still larger than 5% whereas the relative discrepancy in the frequency ν_f never exceeds 0.2%. Despite these unsatisfactory results, the critical Rayleigh number, Ra_c , predicted with only one step of the Lagrange method, namely a linear interpolation, provides an accurate guess of the reference threshold $Ra_{c_{ref}}$. It should be noted that $Ra_{c_{ref}}$ is almost identical by computing it with a linear approximation of the $(Ra_c, \Delta t)$ -data for $\Delta t \rightarrow 0$ or by using a linear interpolation of the reference growth rates between $Ra = 19,000$ and $Ra = 19,500$.

In order to preserve a sufficient accuracy in the critical parameter evaluation, the maximum value of the time step was $\Delta t = 5 \cdot 10^{-5}$.

2. Spatial Accuracy

The effect of the grid size on the growth rates and threshold values are shown in Tabs. IIIa-IIIc and IV. Taking the spatial second-order approximation of the Navier-Stokes and energy equations into account, the growth rates and frequencies were plotted as a function of $1/N_r^2$ or $1/N_\theta^2$, where N_r and N_θ are the number of meshes in the radial and azimuthal directions. As foreseen, the data fall into a straight line. Therefore, linear fits yield the reference values corresponding to N_r and $N_\theta \rightarrow \infty$.

Except for $R = 1.6$ and $k = 4.5$, tables III and IV show that the growth rates may strongly depend on the grid size. However, the interpolated thresholds are almost insensitive to N_r and N_θ . For example, all the critical Rayleigh number values calculated with a 60×240 meshes differ by less than 1% from $Ra_{c_{ref}}$. Thus, this mesh size was retained for most of the computations discussed in the present paper.

III. RESULTS

The stability results are presented for $1.2 \leq R \leq 3$, $Ra \leq 200,000$ and $Pr = 0.7$.

A. Basic steady flows

The basic steady flows are two-dimensional and were carefully examined in a previous paper³ for $Ra < 10,000$. These different flow patterns are now briefly depicted.

Figure 2 sums up the different stable flow patterns occurring for $Ra < 10,000$ and $1.2 \leq R \leq 3$ with respect to 2D-disturbances. Dual¹⁻³ and triple³ stable solutions are met in the parameter space (Ra, R) . They consist in the common large cell (labeled C^+ , Fig. 3(a)), and possibly one or two superimposed small eddies (flows referenced by C^-C^+ , Fig. 3(b), and $C^+C^-C^+$, Fig. 3(c)) with their mirror counterparts. It is worth pointing out that the C^-C^+ flow is destabilized by the onset of a disturbance that breaks the mirror symmetry of the basic solution³. Therefore, it is essential to simulate the two-dimensional flows in full annular spaces to observe this instability, without using any symmetrical assumption. The last mentioned flow pattern c^+C^+ is intermediate between C^+ and $C^+C^-C^+$ and exists in a narrow (Ra, R) -domain, for small gap annuli ($1.2 \leq R \leq 1.35$) and Rayleigh numbers ($2000 < Ra < \approx 5500$). It consists of a co-rotating eddy at the top of the large cell (Fig. 3(d)).

As mentioned just above, numerous basic flows may exist for a set of the Rayleigh number and radius ratio, and subsequently the 3D-stability analysis should be performed for all these 2D-stable solutions.

We first inquire into the stability of the C^-C^+ flow pattern. As indicated in the chart (Fig. 2), this kind of flow is only 2D-stable for $R < 2$. The growth rates of the dominant perturbations of wavelength $k = 1$ are computed and are then copied out on figure 4(a) as a function of Ra and for $R = 1.2, 1.4, 1.6$ and 1.8 . Figure 4(a) also indicates the stability thresholds obtained for two-dimensional disturbances by the Rayleigh numbers corresponding to the right edges of the rectangular hachured boxes. Although the flows with the C^-C^+ pattern are stable for two-dimensional disturbances ($k = 0$), it exists at least one three-dimensional perturbation with a positive growth rate, for example the perturbation with a wavelength $k = 1$. Thus, the flows with one large cell topped by one eddy, with the mirror images, are obviously always unstable.

Before studying the linear stability of the $C^+C^-C^+$ flow pattern, it is necessary to remind us of the origin of this structure (details are presented in³). For narrow gap annuli,

$R \leq 1.25$, the multicellular flows are a result of a continuous transformation from C^+ to c^+C^+ and then to $C^+C^-C^+$ patterns with the increase of the Rayleigh number value. Just before $R = 1.26$, the stability diagram for the two-dimensional disturbances is highly modified by the appearance of a new branch of stable solutions on which the $C^+C^-C^+$ flow pattern now takes place: the continuous change from C^+ to $C^+C^-C^+$ as a function of Ra is now impossible, on the other hand multiple solutions (C^+ and $C^+C^-C^+$) may now be expected. Figure 4(b) presents the growth rates of the dominant perturbation for the wavelength $k = 1$ as well as the stability regions for 2D disturbances. For $R \geq 1.3$, the $C^+C^-C^+$ flows are clearly always unstable.

Consequently, the only basic solutions used in the next sections consist of one large cell C^+ (Fig. 3(a)) eventually topped by two small eddies when $R \leq 1.25$, with the mirror counterparts.

B. Neutral stability curves

For $R = 1.2$, the linear stability analysis is based upon three kinds of flow patterns: the basic solution evolves continuously from C^+ (Fig. 3(a)) to c^+C^+ (Fig. 3(d)) slightly above $Ra = 1917$ and to $C^+C^-C^+$ (Fig. 3(c)) beyond $Ra \approx 2270$. For $R \geq 1.3$, only the common couple of counter-rotating cells composes the basic flows about which the perturbation analysis is performed.

For $1.2 \leq R \leq 1.4$, the two-dimensional steady flow is destabilized when $Ra > Ra_c(k)$ as illustrated in Fig. 5(a) for $R = 1.2$ and $R = 1.3$. When the wavelength of the three-dimensional disturbances tends towards zero, the stability thresholds for 2D-disturbances³ are recovered. Indeed for $k = 0$, the pitchfork bifurcations at $Ra = 2068$ and $Ra = 2456$ for $R = 1.2$, and then the Hopf bifurcation at $Ra = 6008$ for $R = 1.3$, are well found. Notice that the discontinuities observed along each marginal curve are fictive: it is indeed reasonable to suppose that they are linked by "S"-shaped curves, unfortunately not easy to track with the numerical methods used.

For $1.5 \leq R \leq 1.95$ (Fig. 5(b)), the previous neutral stability curves are fold back to give rise to bounded regions of instability. Above the closed curves, the two-dimensional

flows are stable again until the next transition, for which the critical Rayleigh numbers are one order of magnitude higher than those of the first bifurcation. The area of the bounded instability region decreases with R to finally collapse for $1.95 < R < 2$.

Only the upper marginal curve persists for larger radius ratios. For $2 \leq R \leq 3$, $Ra_c(k)$ increases with R and reaches 151,330 at $R = 3$.

C. Stability diagrams for finite length annuli

Consider now horizontal annuli of finite axial length $A = L/d$, with slip conditions at the end-walls. In such configurations, the basic flow is still two-dimensional. Its stability property is deduced from the neutral curves $Ra_c(k)$ in Figs. 5(a) and 5(b) by extracting the critical Rayleigh number values corresponding to the discrete wavenumbers $k = n\pi/A$, n being an integer. The curves $\min_n(Ra(k = n\pi/A))$ or $\max_n(Ra(k = n\pi/A))$ are plotted in Fig. 6, whether the transitions are destabilizing or not, for odd (dashed lines) and even (continuous lines) integers n . If both odd and even multiples of the wavenumber π/A can develop in an annulus of axial aspect ratio A , the effective threshold for the 2D-steady flow destabilization is given by the lowest value of each transition. In Figure 6, the filled circles and squares located along the even and odd stability curves delimit the gap for the onset of the various marginal modes. For convenience's sake, the notations used to refer to the marginal modes consist in placing side-by-side one or two characters followed by an integer. The rules are:

- "S" or "O" marks out the temporal régime: steady or oscillatory;
- "s" is eventually added if the marginal mode satisfies the same spatial property as the basic flow, namely the mirror symmetry with respect to the vertical (r, z) mid-plane;
- the number differentiates the disturbances with identical temporal régime and spatial property.

In order to distinguish the various transitions, the thresholds are labeled as following:

- Ra_{c_1} is for the first transition, $1.2 \leq R \leq 1.95$;
- Ra_{c_2} corresponds to the reversal transition, $1.95 \geq R \geq 1.5$;

- Ra_{c_3} is for the second transition, $1.5 \leq R \leq 2.24$;
- Ra_{c_4} is for the last instability, $2.3 \leq R \leq 3$.

For $R = 1.2$ (Fig. 6(a)), let us compare first the even stability curve, namely the continuous line, with the results by Dyko *et al.*⁶ displayed by the dotted line. A quite good agreement is highlighted except close to $A = 3$ where the onset of a steady symmetrical disturbance labeled "Ss3" occurs below their marginal curve. In fact, a better agreement can be recovered by considering the second even dominant disturbance, namely the steady symmetrical mode "Ss2" not drawn on Fig. 6(a). Therefore, it can be assumed that Dyko *et al.*⁶ have detected the mode "Ss2" but not the mode "Ss3". Notice that different non-linear flow patterns were identified by Dyko and Vafai^{5,7} in narrow-gap annuli, using three-dimensional numerical simulations: five different supercritical states, including three states with even or odd numbers of transversal rolls in the upper part of the annulus, and two states with longitudinal rolls in the upper region in combination with transversal rolls located between the longitudinal rolls and the primary flow.

From $R = 1.2$ to 1.4 (Figs. 6(a)-6(c)), the shapes of the neutral stability curves are qualitatively similar. The three marginal modes are steady and symmetric. The mode "Ss1" is obtained for very small A -values only, and it collapses when increasing R . The mode "Ss2" is the most often found and it remains almost alone for $R = 1.4$. The mode "Ss3" is obtained within small ranges of A . By considering simultaneously the odd and even multiples of the elementary wavenumber π/A , "Ss2" is the mode which generally drives the onset of the instability.

The three patterns of the marginal disturbances "Ss1", "Ss2" and "Ss3" are characterized by high values of the axial component of the velocity (\bar{w}) which are located at annulus top region (Figs. 7(a)-7(c)). The patterns of the mode "Ss2" (Fig. 7(b)) are in qualitative good agreement with those presented in the linear stability study performed by Choi and Kim¹⁷. The maximal values of the axial velocity are slightly shifted in the azimuthal direction from modes "Ss2" to "Ss1", and the mode "Ss3" is characterized by numerous but smaller structures.

For $1.5 \leq R \leq 1.95$, a bounded instability region ($Ra_{c_1} < Ra < Ra_{c_2}$) clearly appears,

firstly in only one domain ($R = 1.5$, Fig. 6(d)), and then split into several independent sub-domains ($1.8 \leq R \leq 1.95$). For intermediate radius ratios, $1.6 \leq R \leq 1.7$ (Figs. 6(e) and 6(f)), the sub-domains are delimited by odd neutral curves. The marginal modes of the first instability region are mainly governed by the steady symmetrical disturbance "Ss2", except for $R = 1.5$ (Fig. 6(d)) where the oscillatory perturbation "O1", breaking the mirror symmetry of the basic flow, occurs. The disturbance "O1" (Fig. 7(e)) is also evidenced for the second instability region (the upper curves at Ra_{c3}) with the symmetrical oscillatory mode labeled "Os1" (Fig. 7(f)). These two unsteady perturbations have very similar growth rates and alternatively emerge as the leading marginal mode, depending on both R and A .

For $2 \leq R \leq 3$, the bounded unstable regions vanish. The marginal curve is shown in Fig. 6(i) for $R = 2.4$. For $2.24 < R \leq 3$ (transition labeled as Ra_{c4}), the marginal mode "S1" (Fig. 7(d)) is steady but contrary to "Ss1", "Ss2" and "Ss3", it breaks the mirror symmetry of the basic flow. In accordance with the study of the leading perturbations, the second mode is oscillatory and corresponds to the mode "O1".

D. Three-dimensional simulations

1. Comparisons with linear stability results

Flow fields computed by solving the unsteady, three-dimensional governing equations (Eq. 1) with slip boundary conditions at the end-walls are discussed in this section.

The growth rates of the axial component of the velocity obtained either by 3D simulations or by the linear stability analysis are reported in Tab. V for $R = 1.8$. Computations were performed for $k = \pi$ and $A = 2$ ($n = 2$) at $Ra_{c1} \pm 5\%$, $Ra_{c2} \pm 5\%$ and $0.5 \times (Ra_{c1} + Ra_{c2})$, and they were initialized by the fluid at rest conditions when the growth rates of the linear stability analysis were negative and, otherwise by the steady three-dimensional flow obtained either at $Ra_{c1} - 5\%$ or at $Ra_{c2} + 5\%$. The succession of 2D-stable, 2D-unstable and the reverse transition to 2D stable flows was confirmed. The relative difference between the growth rates λ evaluated by the two methods was systematically less than 5.5%. It is worth noting that

the evaluation of λ through 3D-computations is much more expensive and, generally provides less accurate values owing to the small but finite amplitude perturbations.

The second destabilization is experienced for $Ra = 22,000 > Ra_{c_3} = 19,962$, $R = 1.7$ and $A = 1.96$ which corresponds to the critical wavenumber $k = 2\pi/A \approx 3.2$ ($n = 2$). In accordance with the stability analysis, the flow is three-dimensional and oscillatory with a frequency $\nu_f \approx 7.96$, a value very close to $\nu_{f_{c_3}} = 8.03$. Favorable qualitative comparisons of the axial components of velocity, obtained either by 3D-computations or by linear stability analysis at the transition (pattern "Os1") are shown in Fig. 8. Note that the numerical simulation was carried out for a Rayleigh number slightly greater than Ra_{c_3} because the growth rate at the transition threshold being negligibly small, the computation time should have been highly expensive.

2. Influence of the boundary conditions at the end walls

This section deals with the effects of no-slip boundary conditions at the end walls on the onset of thermal instabilities for moderate aspect ratio. The aim is to assess the relevance of the stability results provided by the perturbation analysis conducted for slip conditions at the end-walls. The first transition is particularly interesting because of the existence of disconnected instability regions for large enough radius ratios. Four computations, initialized by rest conditions, were thus performed, for $R = 1.9$ and various couples (Ra , A).

The simulations B , D and E shown in Fig. 9 (enlargement of Fig. 6(h)) were carried out for $Ra = 4000$ and $A = 3.5$, $A = 4.4$ and $A = 4.9$. The simulation C was also performed for $A = 4.4$ but for $Ra = 3000$. The flow fields are plotted in Fig. 10 through velocity fields and isothermal patterns in the vertical upper (r, z) -plane. A strong thermal convection motion, produced by two couples of counter-rotating rolls in the top region of the annulus, is seen for the steady-flow cases B and C . In contrast, the isotherms exhibit a weak 3D-structure in the case $A = 4.4$ and $Ra = 4000$ (flow D) for which the solution can be assumed two-dimensional far enough from the end-walls. Notice that this solution was also achieved by starting the computation from the 3D-flow pattern of case C . The boundary rolls are due to the viscous shear layers associated with the no-slip boundary conditions but not to a

thermal instability. The E -flow structure is oscillatory with a dimensionless period $\tau = 30$. It evolves alternatively between two and three couples of counter-rotating cells.

The flow structures exhibit thermal instabilities at the annulus top region, except for case D . The two rolls due to the dynamical boundary conditions as well as the small annular length enforce the fluid flow to satisfy the symmetry with respect to the mid (r, θ) - plane. Consequently, the disturbances with 5 cells cannot develop. The present simulations show therefore fully 3D-patterns for parameters lying in regions bounded by the continuous lines whereas the flow is essentially 2D outside of these regions. This finding may suggest that the stability of the 3D flows with no-slip conditions at the end-walls satisfy the stability requirements displayed in Fig. 9, but only for perturbations with an even number of cells along the axial direction. These results are consistent with the earlier findings of Dyko *et al.*⁶ for moderate gap annuli, specifically that due to the viscous shearing effects of the end-walls, only an even number of rolls forms in the annulus.

Two remarks are added to conclude this section. First, the oscillatory behavior of flow E was not predicted by the steady marginal disturbance "Ss2" at the transition. Secondly, the end-walls in finite length annuli do not generate finite amplitude perturbations able to systematically destabilize 2D-steady flows for parameter sets close to case D .

E. Stability diagram for infinite length annuli

The transition thresholds for infinite length annuli are now presented as a function of the radius ratio. The basic flows at the transitions only consist of the C^+ pattern (see Fig. 3(a)) with its mirror counterpart. For a fixed R -value, the critical parameter $Ra_c(R)$ is analytically calculated by using a quadratic polynomial approximation of $Ra_c(k)$ in the vicinity of the absolute extrema such that $Ra_c(R) = \min_k(Ra_c(k))$ or $Ra_c(R) = \max_k(Ra_c(k))$ for thresholds corresponding to direct transitions or to reverse transitions to stable flows. The critical Rayleigh number values $Ra_c(R)$ are plotted in Fig. 11 as a function of $\sigma = 2r_i^*/d = 2/(R-1)$ (bottom abscissa axis) or as a function of R (top abscissa axis). It should be noted that parameter σ was widely used in previous works instead of R . The ranges of the radius ratio and Rayleigh number values where the four transitions occur are as follows:

- for $1.2 \leq R \leq 1.95$ and $1734 \leq Ra_{c_1} \leq 2894$;

- for $1.95 \geq R \geq 1.5$ and $3643 \leq Ra_{c_2} \leq 13,540$;
- for $1.5 \leq R \leq 2.24$ and $17,130 \leq Ra_{c_3} \leq 52,000$;
- for $2.3 \leq R \leq 3$ and $110,040 \leq Ra_{c_4} \leq 151,330$.

Notice that a curve similar to the Ra_{c_1} -curve shown in Fig. 11 was already obtained by Yoo¹. It indicated the Rayleigh number beyond which the C^-C^+ steady solutions occur, that is the 2D-transition threshold corresponding to a saddle-node bifurcation as demonstrated by Mizushima *et al.*² and later by Petrone *et al.*³. Let also recall that these C^-C^+ steady solutions are always unstable with respect to three-dimensional disturbances (see Sec. III A). Thus, although these Rayleigh number values are close to Ra_{c_1} , they characterize in no way the onset of a disturbance for the usual couple of counter-rotating cells.

For $R < 2$ and $Ra < Ra_{c_1}$, low speed velocities are seen at the top region of the annulus so that a conductive régime is nearly expected. Since the radius ratio is small, the cylinder surfaces are locally almost parallel and horizontal at the top of the annular space where a Rayleigh-Bénard like instability occurs. This instability is illustrated by the axial velocity of the marginal mode "Ss2" at the first transition, for $R = 1.6$ (Fig. 12(a)). This disturbance consists of transverse rolls with an axial wavenumber close to π (see Fig. 13). The onset of the transversal upper eddies depends not only on the local curvature of the walls but also on the Rayleigh number. At the annulus top region, the azimuthal velocity increases indeed with Ra and then stretches out the transversal convective perturbations towards the lateral region when the flow particles are close to the outer cylinder (Fig. 12(b)). This stretching effect produced by the basic flow probably explains the reason for the instability damping. On the other hand, the increase of the radius ratio deteriorates the conditions where the Rayleigh-Bénard like instability may occur by decreasing the angular sector where the wall cylinders may reasonably be considered as parallel and horizontal. Finally, just beyond $R = 1.95$, the curvature is so pronounced that the onset of the thermal instability can no more develop under the shape of two counter-rotating transversal eddies. The axial wavenumber of the disturbance for the reversal transition increases linearly with $\sigma = 2/(R - 1)$ from $k_{c_2} = 3.60$ at $R = 1.9$ to $k_{c_2} = 5.09$ at $R = 1.5$ (Fig. 13). Above Ra_{c_2} , the two-dimensional flow is anew stable.

The transition at Ra_{c_3} (Fig. 11) is due to the onset of the oscillatory mode "Os1" (see for instance Fig. 7(f)). The frequency (Fig. 14) is almost doubled from $\nu_{f_{c_3}} = 7.09$ at $R = 1.5$ to $\nu_{f_{c_3}} = 13.06$ at $R = 2.24$. The wavenumber k_{c_3} does not change monotonously with R but remains close to π (Fig. 13): the maximum value is reached for $R \approx 2$ ($k_{c_3} = 3.43$).

The last bifurcation Ra_{c_4} (Fig. 11) is associated with the dissymmetrical steady perturbation "S1" (see for instance Fig. 7(d)). The wavenumber $k_{c_4} = 5.25$ for $R \approx 2.3$ decreases slowly with R ($k_{c_4} = 5.06$ for $R = 3$).

The instability threshold Ra_{c_1} was previously discussed in the archival literature. It was firstly studied by Mojtabi and Caltagirone^{15,16} and more recently by Choi and Kim¹⁷ and Dyko *et al.*⁶. Figure 15 shows comparison between Ra_{c_1} and the critical Rayleigh numbers reported in^{15,16} by using linear and energetic stability analyses. Except for the smallest radius ratios, the present critical values differ substantially from those reported in^{15,16} when R increases. The discrepancy is due to the assumptions introduced in their analytical model. An approximation function is also displayed in Fig. 15. It reads

$$Ra_1(R) = \frac{1072 R - 2398}{0.7069 R - 1.485} \quad (4)$$

and fits Ra_{c_1} with a relative error not exceeding 1.4% for $1.2 \leq R < 2$. With this approximated function, the Rayleigh-Bénard threshold corresponding to horizontal differentially heated plates ($R = 1$) is recovered within 0.25%, only. Table VI shows the excellent agreement of Ra_{c_1} and k_{c_1} between the present results and those by Choi and Kim¹⁷ calculated by using a spectral method. The relative difference does not exceed 1.5% and 1%, respectively. For $R = 2$, Choi and Kim¹⁷ did not obtain any critical threshold in accordance with the present work showing that the first transition disappears just before $R = 2$. According to¹⁷, the disturbances are oscillatory and are damped for all Ra -values studied ($Ra \leq 100,000$). In particular, the growth rate and the frequency were found equal to $\lambda = -1.055$ and $\nu_f = 60.9/(2\pi) = 9.69$ for $Ra = 25,000$ and $k = 3.3$. This last result does not agree with our findings. We obtained indeed another transition at $Ra_{c_3} = 24,621$ (Fig. 11) with $k_{c_3} = 3.43$ (Fig. 13). To investigate the reason of such a difference, the same computation as in Choi and Kim¹⁷ was carried out. Although the frequency $\nu_f = 9.64$ of our computed leading disturbance is very close to that found by Choi and Kim¹⁷, the growth rate is positive $\lambda = 8.9 \cdot 10^{-2}$ and thus very different from the growth rate reported

in their paper ($\lambda = -1.055$).

Simple analytical functions were sought to define relations between the critical Rayleigh numbers and the radius ratios. The critical Rayleigh numbers $Ra_{c_i}(R)$ are approximated by the function $Ra_i(R)$, for $i = 1$ to 4:

- for $1.2 \leq R \leq 1.95$, $Ra_1(R) = (1072R - 2398)/(0.7069R - 1.485)$ with $|Ra_{c_1} - Ra_1|/Ra_{c_1} < 1.4\%$;
- for $1.95 \geq R \geq 1.5$, $Ra_2(R) = 10,440/(R - 1) - 7300$ with $|Ra_{c_2} - Ra_2|/Ra_{c_2} < 2\%$;
- for $1.5 \leq R \leq 2.24$, $Ra_3(R) = 52,000 - 37,400 \times (2.24 - R)^{0.244}$ with $|Ra_{c_3} - Ra_3|/Ra_{c_3} < 4\%$;
- for $2.3 \leq R \leq 3$, $Ra_4(R) = 59,100R - 27,300$ with $|Ra_{c_4} - Ra_4|/Ra_{c_4} < 1.4\%$.

F. Comparisons with numerical and experimental studies

Many experimental results but few three-dimensional numerical solutions were reported in the literature. The most quoted results are drawn in the present stability chart (Fig. 11). The filled and open symbols correspond to three- and two-dimensional flows, respectively, while the half-filled circles are for parameter values for which both 2D- and 3D- solutions were observed. The stability chart by Powe *et al.*¹⁰ is also drawn in Fig. 11.

The present linear stability analysis is in excellent agreement with the Choi and Kim's results¹⁷ for $1.2 \leq R < 2$ and also with the works by Mojtabi and Caltagirone^{15,16} and by Dyko *et al.*⁶ for narrow-gap annuli. Beyond the critical value Ra_{c_1} , the transverse eddies at the top of the annular space grow and the solution converges toward a non-linear state consisting of a spiral flow as observed in many numerical and experimental studies^{6-8,11}. Although the Ra_{c_1} -curve is in agreement with the Powe's chart for moderate radius ratios ($1.23 \leq R \leq 1.71$), discrepancies appear for smaller-gap annuli ($R \leq 1.23$) where the threshold values are from twice to almost four times larger compared with our results (Fig. 11). According to Powe *et al.*¹⁰, multi-cellular flows take place above the transition. Although our linear stability analysis indicates that the 2D multi-cellular flows are unstable,

Dyko and Vafai⁵ showed longitudinal rolls in the top portion of the annuli for $R \leq 1.15$, but in combination with transverse rolls between the longitudinal rolls and the main flow. As a matter of fact, the curves in the Powe's chart delimit non-linear states and then the comparison with the linear stability thresholds can only be qualitative. Both sub-critical bifurcations and the possible existence of multiple non-linear flows for the same set of parameters may explain such discrepancies.

For moderate radius ratios ($1.5 < R < 2$), the successive transitions reported in the present study, and more specifically the two-dimensional stable region for large Rayleigh number values ($Ra_{c_2} < Ra < Ra_{c_3}$), are not mentioned in the chart by Powe *et al.*¹⁰, except the first transition at Ra_{c_1} . However, the experimental works by Grigull and Hauf⁹ reported that three- or two-dimensional flows can exist in the ranges $1.3 \leq R \leq 6.3$ and $1680 \leq Ra \leq 21,000$. Recent three-dimensional numerical simulations for $R = 1.7$ and $Ra = 10,000$ ⁸ (half-filled circle in Fig. 11) also showed flows either essentially two-dimensional or fully three-dimensional as a function of the initial conditions.

At a first sight, the onset of the second instability at Ra_{c_3} seems to be in disagreement with the experimental results by Grigull and Hauf⁹ who reported a reversal transition to two-dimensional flows occurring above $Ra = 21,000$, for $1.3 \leq R \leq 6.3$. This noticeable contradiction can be raised by considering the three-dimensional numerical simulations performed by Petrone *et al.*⁸ for $R = 1.7$ and $Ra = 22,000 > Ra_{c_3}$ (half-filled circle in Fig. 11). Indeed, they proved that the choice of a too small aspect ratio ($A = 6$) damps the instability onset and therefore the flow remains steady and essentially two-dimensional in the core flow region. Although for a larger aspect ratio ($A = 20$), the flow is oscillatory with a frequency $\pi\nu_f = 25$ and a characteristic wavelength $k = \pi n/A = 3.45$, both in good agreement with the frequency $\pi\nu_{f_{c_3}} = 25.23$ (Fig. 14) and the wavelength $k_{c_3} = 3.2$ (Fig. 13) at the transition, the axial component of the velocity is very small. Thus, either a too small aspect ratio or the existence of a small axial velocity, probably hard to be experimentally observed or measured, may explain the results by Grigull and Hauf⁹, namely the assumed two-dimensionality of the flows.

The last transition Ra_{c_4} is correctly represented by the marginal curve proposed by Powe *et al.*¹⁰ in their stability chart. Despite this qualitative agreement, the transitions differs:

2D-oscillatory flows versus 3D-steady disturbances. However, in both cases, perturbations and experimental flows break the mirror symmetry of the counter-rotating basic flow cells. The resulting flow consists in an oscillatory thermal plume in each (r, θ) -plane as recently confirmed in the experiments by Labonia *et al.*¹³ and in three-dimensional numerical simulation by Petrone *et al.*¹⁴ (filled squares above Ra_{c_4} in Fig. 13). It can be noticed that the second leading mode at the transition Ra_{c_4} is oscillatory, breaks the mirror symmetry of the basic flow and corresponds to the mode labeled "O1". The superimposition of this disturbance and of the basic flow permits to recover the oscillation of the thermal plume. The bifurcation at Ra_{c_4} is therefore probably subcritical.

IV. CONCLUSION

Three-dimensional linear stability analyses of two-dimensional natural convection flows in air-filled horizontal annuli were performed for radius ratios in the range $1.2 \leq R \leq 3$. New transitions were highlighted for moderate and large radius ratios. It was emphasized that 2D-flows may be stable for $1.5 \leq R < 2$, i.e. above the first instability threshold reported in the literature. The basic solution is therefore destabilized by an oscillatory disturbance for a Rayleigh number value one order of magnitude higher than the first transition. For larger radius ratios ($R \geq 2.3$), the crescent-shaped flow is stable for large Ra -values, up to 10^5 . The flow transitions are thus through disturbances breaking the symmetry of the base flow. Such transitions were evidenced for infinite and finite length annuli with slip boundary conditions at the end-walls. The effect of no-slip conditions on the first instability region was also investigated by three-dimensional simulations. The wavelengths of disturbances corresponding to odd submultiples of the annular length did not develop in small length annuli. Finally, the disturbances and critical Rayleigh numbers were compared and discussed with experimental results and three-dimensional numerical simulations reported in the literature.

To conclude, natural convection flows in horizontal annuli can be classified into three categories according to the value of the radius ratio. Transverse, steady roll perturbations are amplified at $Ra_c \approx 2000$ in narrow-gap annuli with $R < 1.5$. Moderate-gap annuli are defined by radius ratios at which multiple transitions occur for the two-dimensional flows, namely for $1.5 < R < 2$. Large-gap annuli, $R > 2$, are associated with onset of oscillatory disturbances for $2 < R < 2.24$ and $Ra = \mathcal{O}(10^4)$, and with steady, symmetrical breaking

disturbances for $R > 2.24$ and $Ra = \mathcal{O}(10^5)$.

Acknowledgments

This work was supported in part by the french computational center (Institute for Development and Resources in Intensive Scientific computing) through Grant N° 051265.

* Present adress: University of Catania, Dipartimento di Ingegneria Industriale e Meccanica, V.le A. Doria 6, 95125 CATANIA, Italy

† Electronic address: `eric.chenier@univ-mlv.fr`

- ¹ J. Yoo, “Dual steady solutions in natural convection between horizontal concentric cylinders”, *Int. J. Heat Fluid Flow* **17**, 587 (1996).
- ² J. Mizushima, S. Hayashi, and T. Adachi, “Transitions of natural convection in a horizontal annulus”, *Int. J. Heat Mass Transfer* **44**, 1249 (2001).
- ³ G. Petrone, E. Chénier, and G. Lauriat, “Stability of free convection in air-filled horizontal annuli: Influence of the radius ratio”, *Int. J. Heat Mass Transfer* **47**, 3889 (2004).
- ⁴ C. Liu, W. K. Mueller, and F. Landis, “Natural convection heat transfer in long horizontal cylindrical annuli”, *ASME Int. Developments in Heat Transfer* **5**, 976 (1961).
- ⁵ M. Dyko and K. Vafai, “On the presence of odd transverse convective rolls in narrow-gap horizontal annuli”, *Phys. Fluids* **14**, 1291 (2002).
- ⁶ M. Dyko, K. Vafai, and A. Mojtabi, “A numerical and experimental investigation of stability of natural convective flows within a horizontal annulus”, *J. Fluid Mech.* **381**, 27 (1999).
- ⁷ M. Dyko and K. Vafai, “Three-dimensional natural convective states in a narrow-gap horizontal annulus”, *J. Fluid Mech.* **445**, 1 (2001).
- ⁸ G. Petrone, E. Chénier, and G. Lauriat, “Three-dimensional study of multiple transitions for natural convection in horizontal annuli”, *Int. J. Heat Mass Transfer* **49**, 1231 (2006).
- ⁹ U. Grigull and W. Hauf, “Natural convection in horizontal cylindrical annuli”, in *Proc. of the third Int. Heat Transfer Conference, Paper No 60* (AIChE, 1966), vol. 2, pp. 182–195.
- ¹⁰ R. Powe, C. Carley, and E. Bishop, “Free convective flow patterns in cylindrical annuli”, *Trans. ASME C: J. Heat Transfer* **91**, 310 (1969).

- ¹¹ Y. Rao, Y. Miki, K. Fukuda, Y. Takata, and S. Hasegawa, “Flow patterns of natural convection in horizontal cylindrical annuli”, *Int. J. Heat Mass Transfer* **28**, 705 (1985).
- ¹² E. Bishop and C. Carley, “Photographic studies of natural convection between concentric cylinders”, in *Proc. Heat Transf. Fluid Mech. Inst.* (Stanford Calif.: Stanford University Press, 1966), pp. 63–78.
- ¹³ G. Labonia and G. Guj, “Natural convection in a horizontal concentric cylindrical annulus: oscillatory flow and transition to chaos”, *J. Fluid Mech.* **375**, 179 (1998).
- ¹⁴ G. Petrone, “Etude numérique des écoulements de convection naturelle et mixte dans un espace annulaire horizontal : approche par analyse de stabilité linéaire”, Ph.D. thesis, University of Marne-la-Vallée (2004).
- ¹⁵ A. Mojtabi and J. P. Caltagirone, “Etude de la stabilité d’un écoulement de convection naturelle dans un espace annulaire horizontal”, *J. de Mécanique* **18**, 225 (1979).
- ¹⁶ A. Mojtabi and J. P. Caltagirone, “Energy stability of a natural convective flow in a horizontal annular space”, *Phys. Fluids* **22**, 1208 (1979).
- ¹⁷ J. Choi and M.-U. Kim, “Three-dimensional linear stability of natural convective flow between concentric horizontal cylinders”, *Int. J. Heat Mass Transfer* **36**, 4173 (1993).
- ¹⁸ Reprinted from Publication *Int. J. Heat Mass Transfer* **47**, G. Petrone, E. Chénier, and G. Lauriat, “Stability of free convection in air-filled horizontal annuli: Influence of the radius ratio”, 3889–3907, Copyright (2004), with permission from Elsevier.

(a) $R = 1.2$, $Ra = 2000$ and $k = 3$

Δt	λ	$\frac{\lambda - \lambda_{ref}}{\lambda_{ref}}$
$5 \cdot 10^{-3}$	1.4539	9.95%
$5 \cdot 10^{-4}$	1.5969	1.09%
$5 \cdot 10^{-5}$	1.6136	0.06%
$5 \cdot 10^{-6}$	1.6153	0.04%
$\Delta t \rightarrow 0$	$\lambda \rightarrow \lambda_{ref}$ 1.6153	0%

(b) $R = 1.6$, $Ra = 10,000$ and $k = 4.5$ (c) $R = 2.6$, $Ra = 124,500$ and $k = 5$

Δt	λ	$\frac{\lambda - \lambda_{ref}}{\lambda_{ref}}$	Δt	λ	$\frac{\lambda - \lambda_{ref}}{\lambda_{ref}}$
$7.5 \cdot 10^{-5}$	$2.309 \cdot 10^{-1}$	0.17%	$7.5 \cdot 10^{-5}$	$-9.520 \cdot 10^{-2}$	0.40%
$5 \cdot 10^{-5}$	$2.310 \cdot 10^{-1}$	0.12%	$5 \cdot 10^{-5}$	$-9.532 \cdot 10^{-2}$	0.27%
$2.5 \cdot 10^{-5}$	$2.311 \cdot 10^{-1}$	0.07%	$2.5 \cdot 10^{-5}$	$-9.545 \cdot 10^{-2}$	0.13%
$1.5 \cdot 10^{-5}$	$2.312 \cdot 10^{-1}$	0.03%	$1.5 \cdot 10^{-5}$	$-9.550 \cdot 10^{-2}$	0.08%
10^{-5}	$2.313 \cdot 10^{-1}$	0.02%	10^{-5}	$-9.553 \cdot 10^{-2}$	0.05%
$\Delta t \rightarrow 0$	$\lambda \rightarrow \lambda_{ref}$ $2.313 \cdot 10^{-1}$	0%	$\Delta t \rightarrow 0$	$\lambda \rightarrow \lambda_{ref}$ $-9.558 \cdot 10^{-2}$	0%

Table I: Influence of the time step on the growth rate.

	$\lambda + i2\pi\nu_f$ $\left(\frac{ \lambda - \lambda_{ref} }{ \lambda_{ref} } + i \frac{ \nu_f - \nu_{f_{ref}} }{ \nu_{f_{ref}} } \right)$		Ra_c $\left(\frac{ Ra_c - Ra_{c_{ref}} }{ Ra_{c_{ref}} } \right)$
Δt	$Ra = 19,000$	$Ra = 19,0500$	
$7.5 \cdot 10^{-5}$	$5.516 \cdot 10^{-3} + 47.68i$ (107.32% + 0.16%i)	$2.810 \cdot 10^{-1} + 48.25i$ (40.48% + 0.16%i)	18,989.99 (0.768%)
$5 \cdot 10^{-5}$	$-2.110 \cdot 10^{-2} + 47.70i$ (72.02% + 0.10%i)	$2.539 \cdot 10^{-1} + 48.27i$ (26.93% + 0.10%i)	19,038.36 (0.515%)
$2.5 \cdot 10^{-5}$	$-4.777 \cdot 10^{-2} + 47.74i$ (36.65% + 0.05%i)	$2.267 \cdot 10^{-1} + 48.31i$ (13.36% + 0.05%i)	19,087.01 (0.261%)
$1.5 \cdot 10^{-5}$	$-5.849 \cdot 10^{-2} + 47.74i$ (22.43% + 0.03%i)	$2.157 \cdot 10^{-1} + 48.31i$ (7.84% + 0.03%i)	19,106.66 (0.158%)
10^{-5}	$-6.415 \cdot 10^{-2} + 47.74i$ (14.92% + 0.02%i)	$2.113 \cdot 10^{-1} + 48.31i$ (5.62% + 0.02%i)	19,116.46 (0.107%)
$5 \cdot 10^{-6}$	$-7.136 \cdot 10^{-2} + 47.75i$ (5.36% + 0.01%i)	$2.044 \cdot 10^{-1} + 48.32i$ (2.19% + 0.01%i)	19,129.38 (0.039%)
$\Delta t \rightarrow 0$	$\lambda + i2\pi\nu_f \rightarrow \lambda_{ref} + i2\pi\nu_{f_{ref}}$ $-7.540 \cdot 10^{-2} + 47.75i$ $2.000 \cdot 10^{-1} + 48.32i$		$Ra_c \rightarrow Ra_{c_{ref}}$ 19,136.88

Table II: Influence of the time step on the growth rate, frequency and Ra_c for $R = 1.6$ and $k = 3.2$.

(a) $R = 1.2$ and $k = 3$

	λ $\left(\frac{ \lambda - \lambda_{ref} }{ \lambda_{ref} }\right)$		$Ra_c \approx Ra^{(3)}$ $\left(\frac{ Ra_c - Ra_{c_{ref}} }{ Ra_{c_{ref}} }\right)$	λ
$N_r \times N_\theta$	$Ra^{(1)} = 1700$	$Ra^{(2)} = 1800$		$Ra^{(3)}$
30×120	$-1.734 \cdot 10^{-1}$ (26.9%)	$4.563 \cdot 10^{-1}$ (16.5%)	1727.54 (0.587%)	$-1.555 \cdot 10^{-3}$
60×240	$-2.214 \cdot 10^{-1}$ (6.76%)	$4.079 \cdot 10^{-1}$ (4.13%)	1735.18 (0.147%)	$1.001 \cdot 10^{-3}$
120×480	$-2.335 \cdot 10^{-1}$ (1.66%)	$3.956 \cdot 10^{-1}$ (1.01%)	1737.11 (0.036%)	$1.493 \cdot 10^{-3}$
$N_r \rightarrow \infty$ $N_\theta \rightarrow \infty$	$\lambda \rightarrow \lambda_{ref}$ $-2.374 \cdot 10^{-1} \mid 3.917 \cdot 10^{-1}$		$Ra_c \rightarrow Ra_{c_{ref}}$ 1737.74	

(b) $R = 2.6$ and $k = 5$

	λ $\left(\frac{ \lambda - \lambda_{ref} }{ \lambda_{ref} }\right)$		$Ra_c \approx Ra^{(3)}$ $\left(\frac{ Ra_c - Ra_{c_{ref}} }{ Ra_{c_{ref}} }\right)$	λ
$N_r \times N_\theta$	$Ra^{(1)} = 124,500$	$Ra^{(2)} = 129,500$		$Ra^{(3)}$
60×240	$-9.532 \cdot 10^{-2}$ (71.63%)	$9.958 \cdot 10^{-1}$ (29.01%)	124,936.82 (0.857%)	$4.91 \cdot 10^{-4}$
80×320	$-1.975 \cdot 10^{-1}$ (41.24%)	$9.014 \cdot 10^{-1}$ (16.77%)	125,398.47 (0.491%)	$4.37 \cdot 10^{-4}$
100×400	$-2.486 \cdot 10^{-1}$ (26.03%)	$8.538 \cdot 10^{-1}$ (10.61%)	125,627.48 (0.308%)	$2.95 \cdot 10^{-4}$
120×480	$-2.774 \cdot 10^{-1}$ (17.45%)	$8.269 \cdot 10^{-1}$ (7.12%)	125,756.11 (0.206%)	$2.80 \cdot 10^{-4}$
$N_r \rightarrow \infty$ $N_\theta \rightarrow \infty$	$\lambda \rightarrow \lambda_{ref}$ $-3.361 \cdot 10^{-1} \mid 7.193 \cdot 10^{-1}$		$Ra_c \rightarrow Ra_{c_{ref}}$ 126,016.5	

(c) $R = 1.6$ and $k = 4.5$

	λ $\left(\frac{ \lambda - \lambda_{ref} }{ \lambda_{ref} }\right)$		$Ra_c \approx Ra^{(3)}$ $\left(\frac{ Ra_c - Ra_{c_{ref}} }{ Ra_{c_{ref}} }\right)$	λ
$N_r \times N_\theta$	$Ra^{(1)} = 10,000$	$Ra^{(2)} = 10,250$		$Ra^{(3)}$
60×240	$2.310 \cdot 10^{-1}$ (0.46%)	$-2.102 \cdot 10^{-1}$ (1.58%)	10,130.91 (0.007%)	$4.48 \cdot 10^{-3}$
80×320	$2.314 \cdot 10^{-1}$ (0.31%)	$-2.120 \cdot 10^{-1}$ (0.52%)	10,130.34 (0.001%)	$3.54 \cdot 10^{-3}$
100×400	$2.316 \cdot 10^{-1}$ (0.20%)	$-2.128 \cdot 10^{-1}$ (0.33%)	10,130.28 (0.001%)	$3.46 \cdot 10^{-3}$
120×480	$2.318 \cdot 10^{-1}$ (0.13%)	$-2.130 \cdot 10^{-1}$ (0.23%)	10,130.27 (0.001%)	$3.44 \cdot 10^{-3}$
$N_r \rightarrow \infty$ $N_\theta \rightarrow \infty$	$\lambda \rightarrow \lambda_{ref}$ $2.320 \cdot 10^{-1} \mid -2.140 \cdot 10^{-1}$		$Ra_c \rightarrow Ra_{c_{ref}}$ 10,130.20	

Table III: Influence of the meshes on the growth rate and Ra_c .

	$\lambda + i2\pi\nu_f$ $\left(\frac{ \lambda - \lambda_{ref} }{ \lambda_{ref} } + i \frac{ \nu_f - \nu_{f_{ref}} }{ \nu_{f_{ref}} } \right)$		$Ra_c \approx Ra^{(3)}$ $\left(\frac{ Ra_c - Ra_{c_{ref}} }{ Ra_{c_{ref}} } \right)$	λ
$N_r \times N_\theta$	$Ra^{(1)} = 19,000$	$Ra^{(2)} = 19,500$		$Ra^{(3)}$
60×240	$-2.110 \cdot 10^{-2} + 47.70i$ (2.30% + 0.09%i)	$2.539 \cdot 10^{-1} + 48.27i$ (0.09% + 0.09%i)	19,038.36 (0.004%)	$1.25 \cdot 10^{-4}$
80×320	$-2.132 \cdot 10^{-2} + 47.72i$ (1.30% + 0.05%i)	$2.540 \cdot 10^{-1} + 48.29i$ (0.05% + 0.05%i)	19,038.71 (0.002%)	$7.53 \cdot 10^{-5}$
100×400	$-2.142 \cdot 10^{-2} + 47.73i$ (0.83% + 0.03%i)	$2.540 \cdot 10^{-1} + 48.30i$ (0.03% + 0.03%i)	19,038.88 (0.002%)	$3.10 \cdot 10^{-4}$
120×480	$-2.147 \cdot 10^{-2} + 47.74i$ (0.57% + 0.02%i)	$2.541 \cdot 10^{-1} + 48.30i$ (0.02% + 0.02%i)	19,038.96 (0.001%)	$2.07 \cdot 10^{-4}$
$N_r \rightarrow \infty$ $N_\theta \rightarrow \infty$	$\lambda + i2\pi\nu_f \rightarrow \lambda_{ref} + i2\pi\nu_{f_{ref}}$ $-2.160 \cdot 10^{-2} + 47.75i$ $2.540 \cdot 10^{-1} + 48.32i$		$Ra_c \rightarrow Ra_{c_{ref}}$ 19,039.16	

Table IV: Influence of the meshes on the growth rate, frequency and Ra_c for $R = 1.6$ and $k = 3.2$.

	λ		
Ra	linear stability	3D-simulation	relative gap
2099.5	$-3.5497 \cdot 10^{-1}$	$-3.5578 \cdot 10^{-1}$	0.23%
2320.5	$3.0947 \cdot 10^{-1}$	$3.0930 \cdot 10^{-1}$	0.05%
3700	1.5894	1.6071	1.10%
4930.5	$4.0314 \cdot 10^{-1}$	$4.1827 \cdot 10^{-1}$	3.62%
5449.5	$-4.3943 \cdot 10^{-1}$	$-4.6380 \cdot 10^{-1}$	5.25%

Table V: Comparisons of the growth rate, λ , achieved by stability analyses and by three-dimensional simulations for $R = 1.8$.

R	Ra_{c_1} $\frac{ Ra_{c_1} - Ra_{c_1}^{ref} }{Ra_{c_1}^{ref}}$	$Ra_{c_1}^{ref}$	k_{c_1} $\frac{ k_{c_1} - k_{c_1}^{ref} }{k_{c_1}^{ref}}$	$k_{c_1}^{ref}$
1.2	1734.6 1.2%	1714.1	3.04 0.15%	3.05
1.3	1764.9 1.4%	1741.1	3.04 0.06%	3.04
1.5	1861.5 1.1%	1842.2	3.04 0.47%	3.03
1.8	2207.6 1.4%	2178.3	3.13 0.87%	3.10
1.9	2514.7 0.2%	2514.5	3.20 0.35%	3.19

Table VI: Comparisons of Ra_{c_1} and k_{c_1} with values reported by Choi and Kim¹⁷ ($Ra_{c_1}^{ref}$, $k_{c_1}^{ref}$).

List of figures

1. Geometry of the annular space.
2. Chart¹⁸ of the two-dimensional flow patterns in the (R, Ra) plane.
3. Flow patterns¹⁸ for $R = 1.2$ (a) $Ra = 1500, C^+$, (b) $Ra = 5000, C^-C^+$, (c) $Ra = 2500, C^+C^-C^+$, (d) $Ra = 2000, c^+C^+$.
4. Growth rates of the dominant perturbation for $k = 1$ and stable regions for two dimensional disturbances (a) basic flow C^-C^+ , (b) basic flow $C^+C^-C^+$.
5. Neutral stability curves as a function of the wavelength and the radius ratio (a) $R = 1.2$ and 1.3 (b) $R = 1.7, 1.8$ and 1.9.
6. Neutral stability curves as a function of A , (a) $R = 1.2$, (b) $R = 1.3$, (c) $R = 1.4$, (d) $R = 1.5$, (e) $R = 1.6$, (f) $R = 1.7$, (g) $R = 1.8$, (h) $R = 1.9$, (i) $R = 2.4$. Marginal modes are noted: "O" for oscillatory and "S" for steady régimes, "s" for patterns satisfying the same spatial property as the basic flow (the mirror symmetry) and the integer distinguishes perturbations with the identical temporal régime and spatial property.
7. Axial component of the velocity disturbances (a) "Ss1", $Ra = 2050, k = 4.4$ and $R = 1.2$, (b) "Ss2", $Ra = 1800, k = 3$ and $R = 1.2$, (c) "Ss3", $Ra = 1850, k = 2$ and $R = 1.2$, (d) "S1", $Ra = 110,000, k = 5$ and $R = 2.4$, (e) "O1", $Ra = 12000, k = 3, R = 1.5$ at t and a quarter of period later, (f) "Os1", $Ra = 20000, k = 3.2, R = 1.7$ at t and a quarter of period later.
8. Comparison between isolines of the axial component of velocity, mode "Os1": three-dimensional simulation at $Ra = 22,000$ and $A = 1.96$ (left) and linear stability analysis at $Ra_{c_3} \approx 20,000$ and $k = 3.25$ (right).
9. Neutral stability curves $Ra_c(A)$ for $R = 1.9$. Points B ($Ra = 4000, A = 3.5$), C ($Ra = 3000, A = 4.4$), D ($Ra = 4000, A = 4.4$) and E ($Ra = 4000, A = 4.9$) indicate the parameters for 3D-numerical simulations.
10. Isotherms and velocity vectors in the upper vertical (r, z) -section. B, C, D and E refer to the dimensionless parameters indicated on the stability chart in Fig. 9.

11. Stability thresholds Ra_c as a function of σ or R , chart by Powe *et al.*¹⁰, numerical and experimental results^{6,8-11,13,14}.
12. Axial component of velocity perturbation ("Ss2") for $R = 1.6$ and close to transitions Ra_{c_1} and Ra_{c_2} , (a) $Ra = 1900$, $k = 3.2$ and (b) $Ra = 10,000$, $k = 4.5$.
13. Critical wavenumber as a function of σ or R .
14. Critical frequency $\nu_{f_{c_3}}$ as a function of σ or R .
15. Comparison of Ra_{c_1} with results of literature^{15,16}; approximation function $Ra_1(R)$.

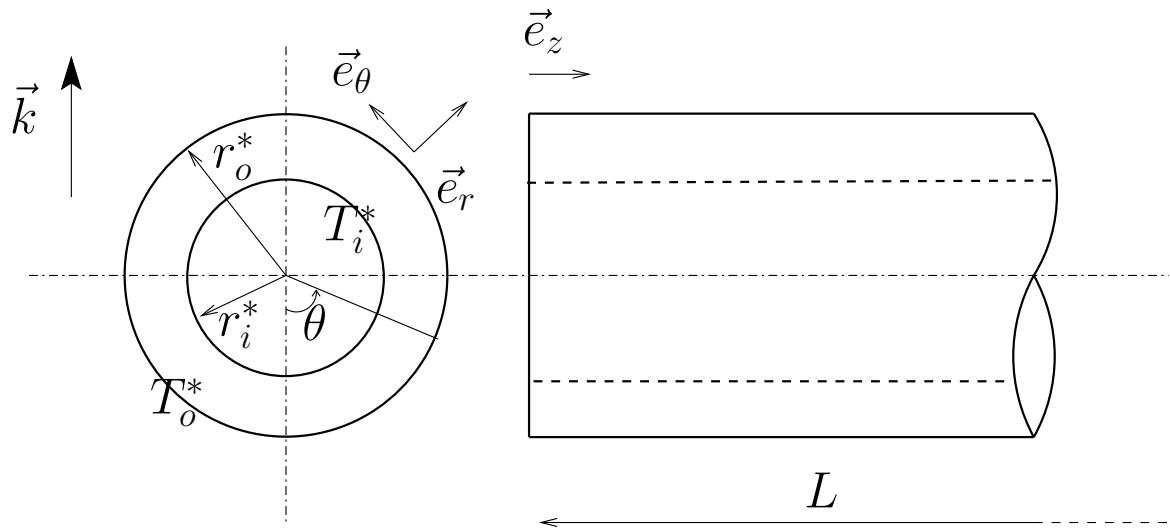


Figure 1: Giuseppe Petrone, Physics of Fluids

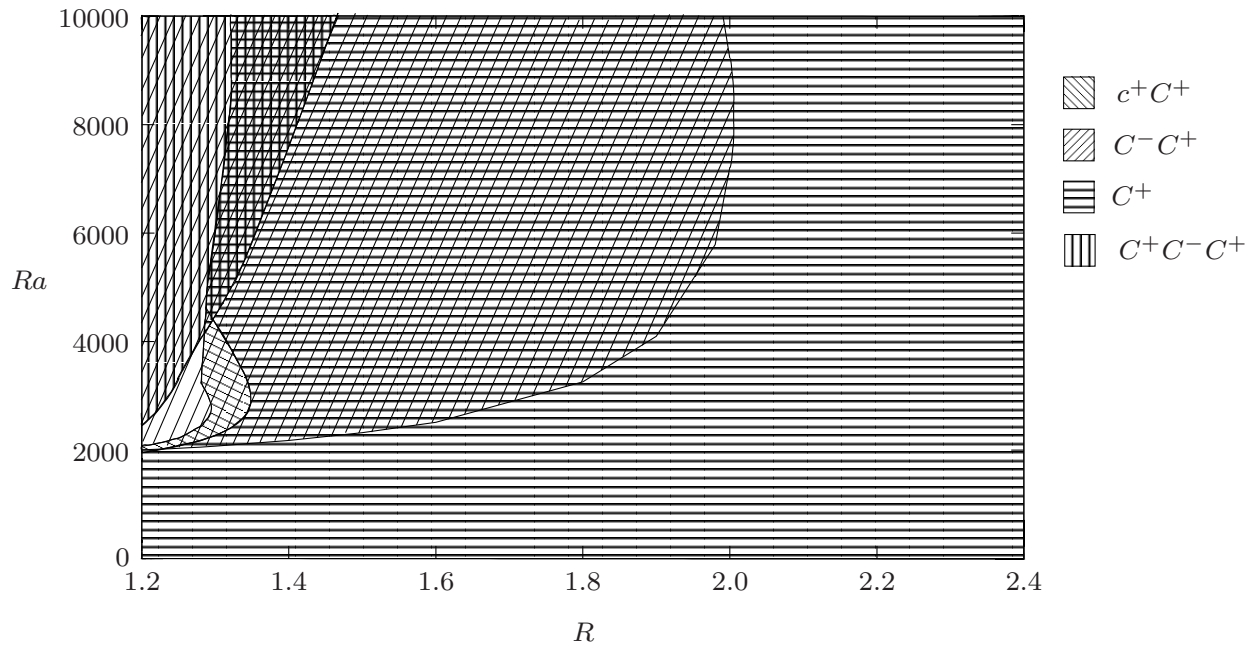


Figure 2: Giuseppe Petrone, Physics of Fluids

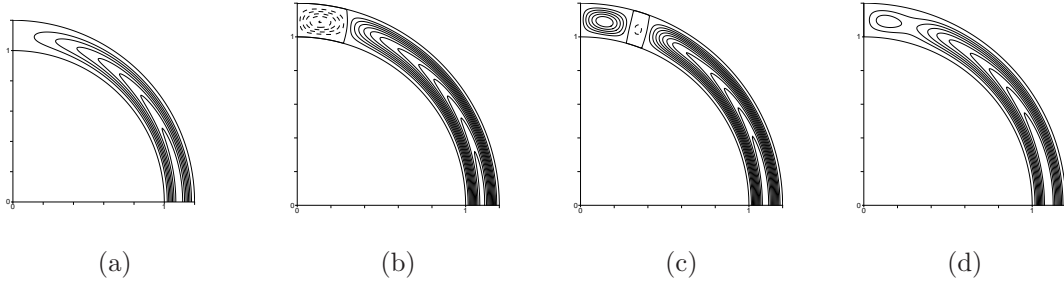
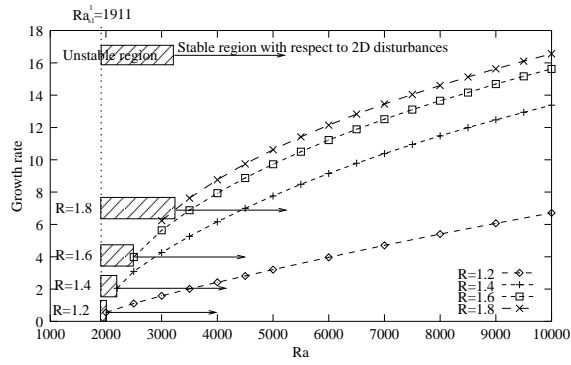
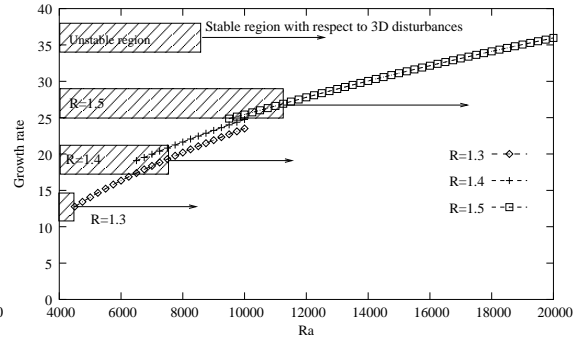


Figure 3: Giuseppe Petrone, Physics of Fluids



(a)



(b)

Figure 4: Giuseppe Petrone, Physics of Fluids

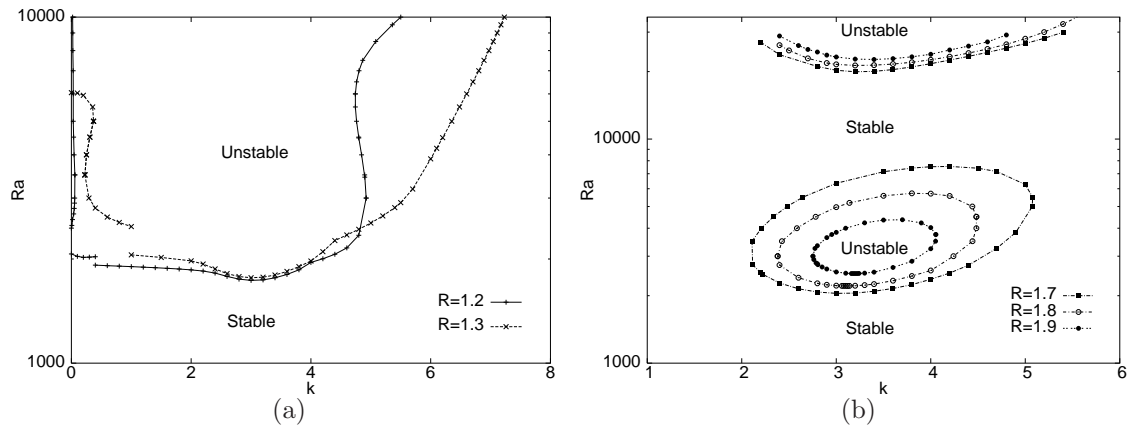


Figure 5: Giuseppe Petrone, Physics of Fluids

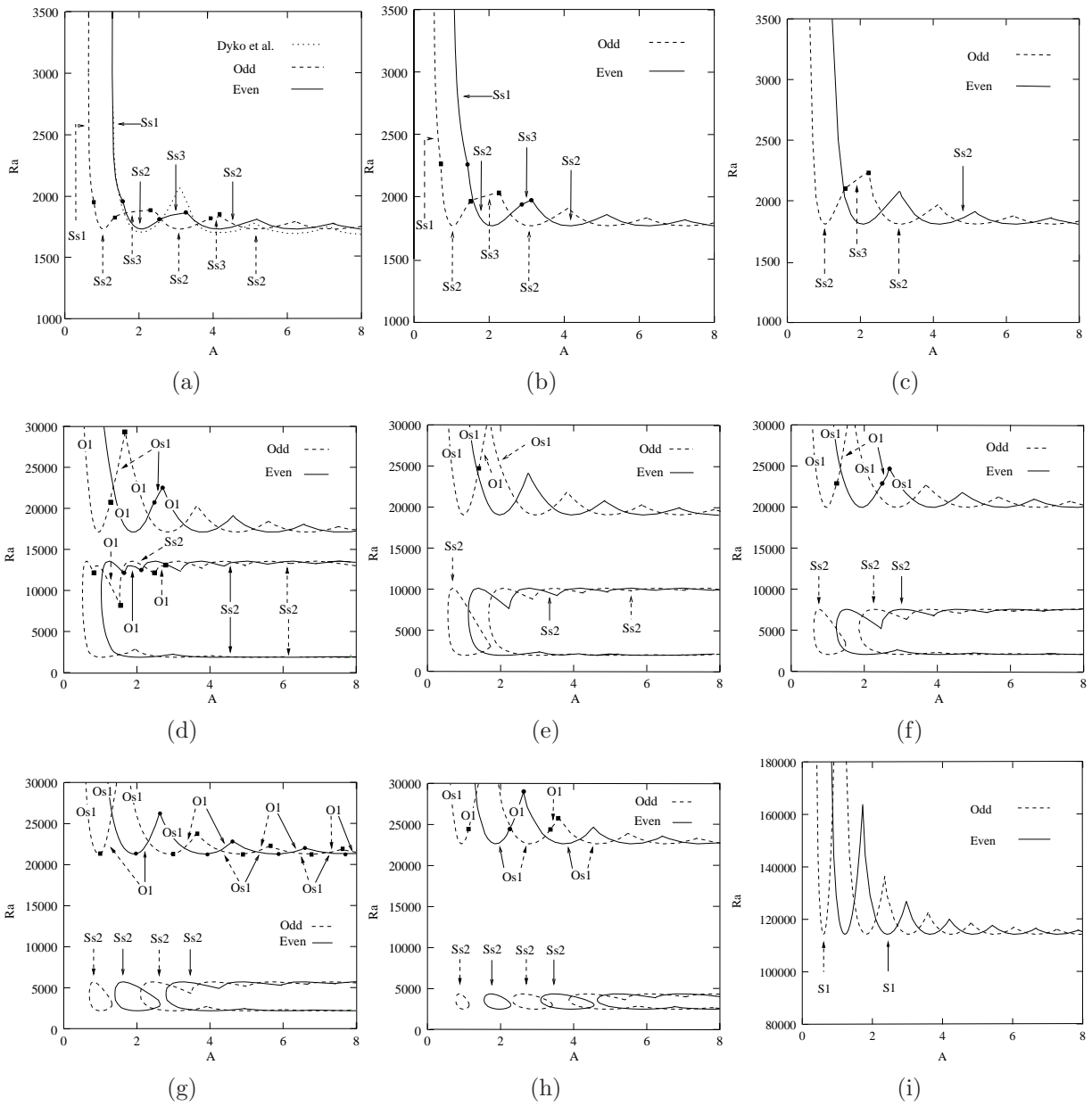


Figure 6: Giuseppe Petrone, Physics of Fluids

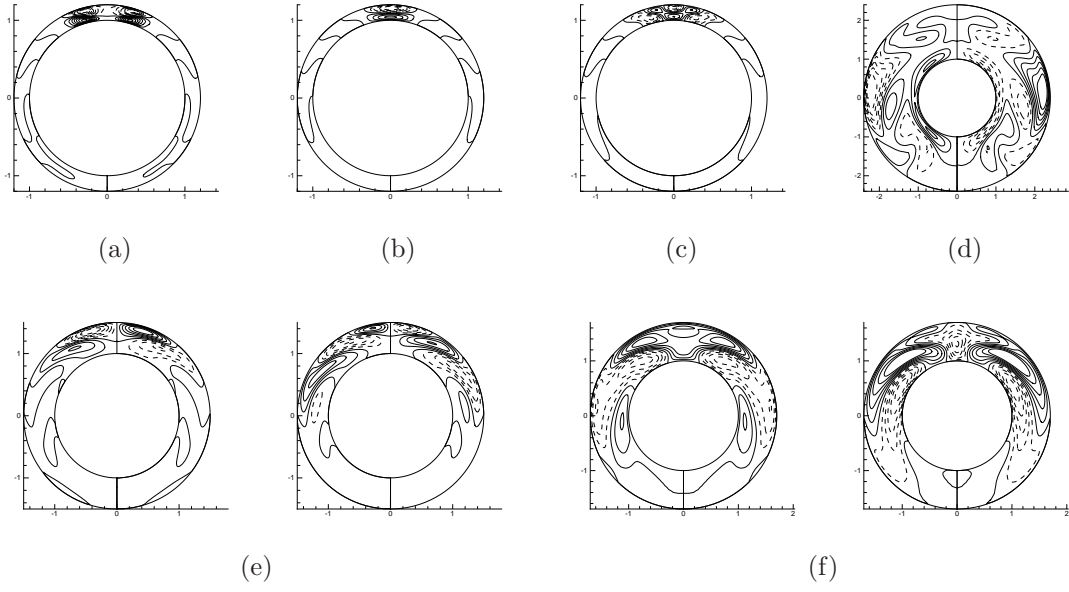


Figure 7: Giuseppe Petrone, Physics of Fluids

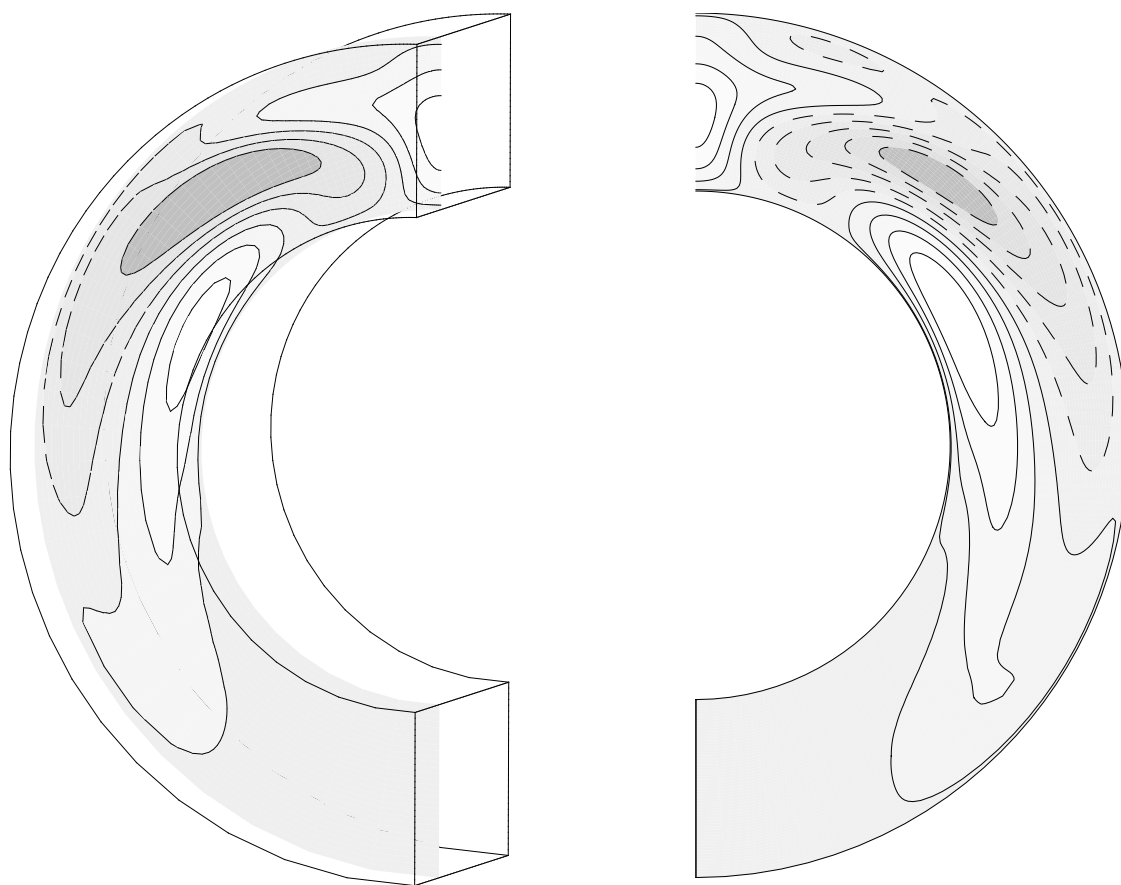


Figure 8: Giuseppe Petrone, Physics of Fluids

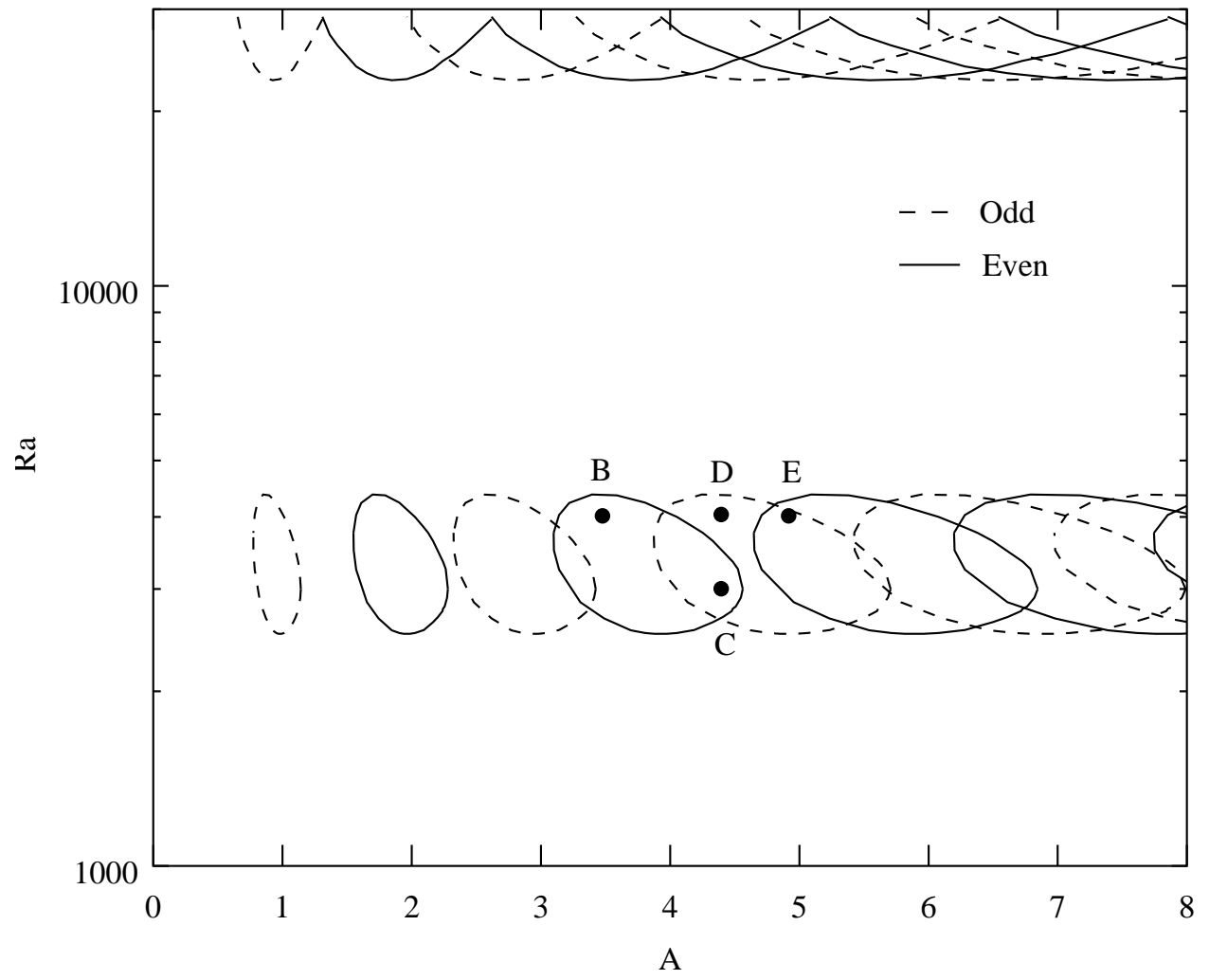
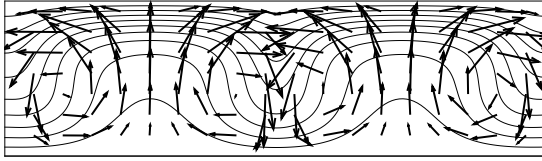
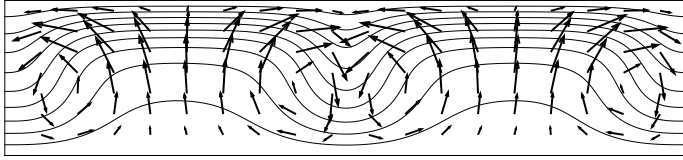


Figure 9: Giuseppe Petrone, Physics of Fluids

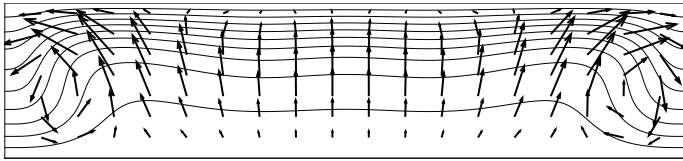
B



C



D



E

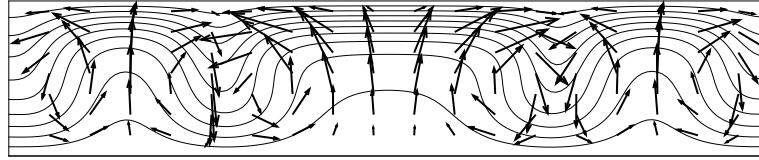
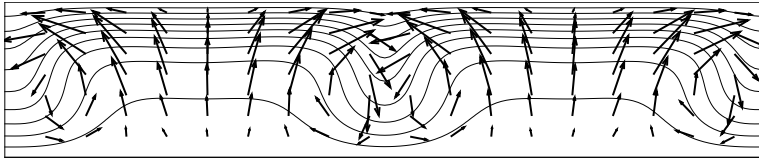


Figure 10: Giuseppe Petrone, Physics of Fluids

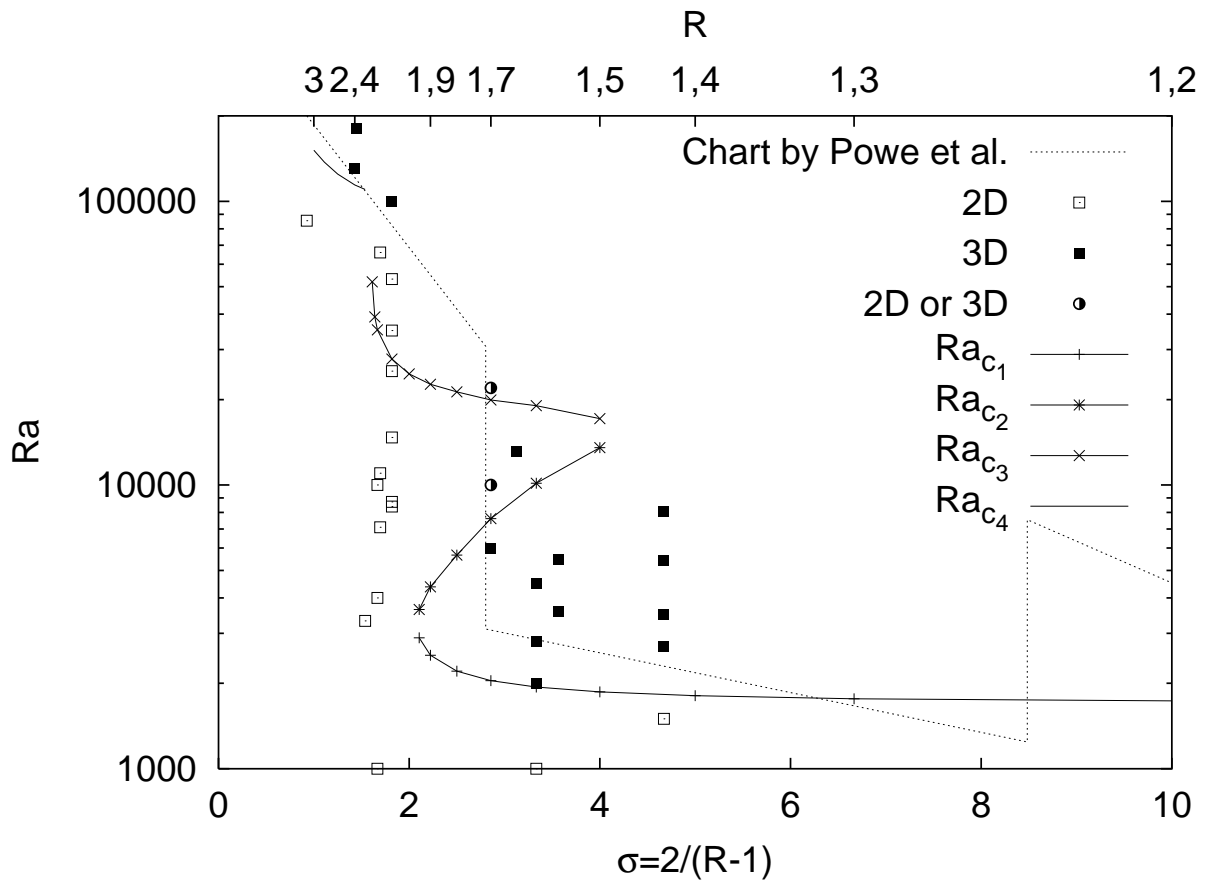
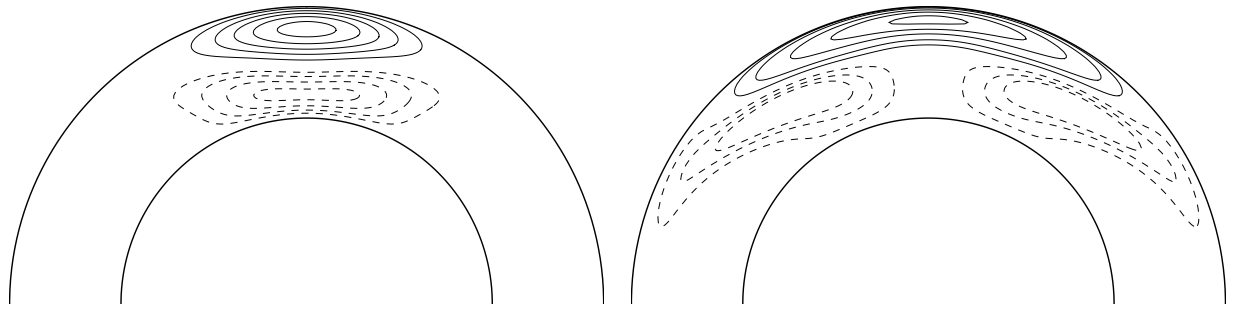


Figure 11: Giuseppe Petrone, Physics of Fluids



(a)

(b)

Figure 12: Giuseppe Petrone, Physics of Fluids

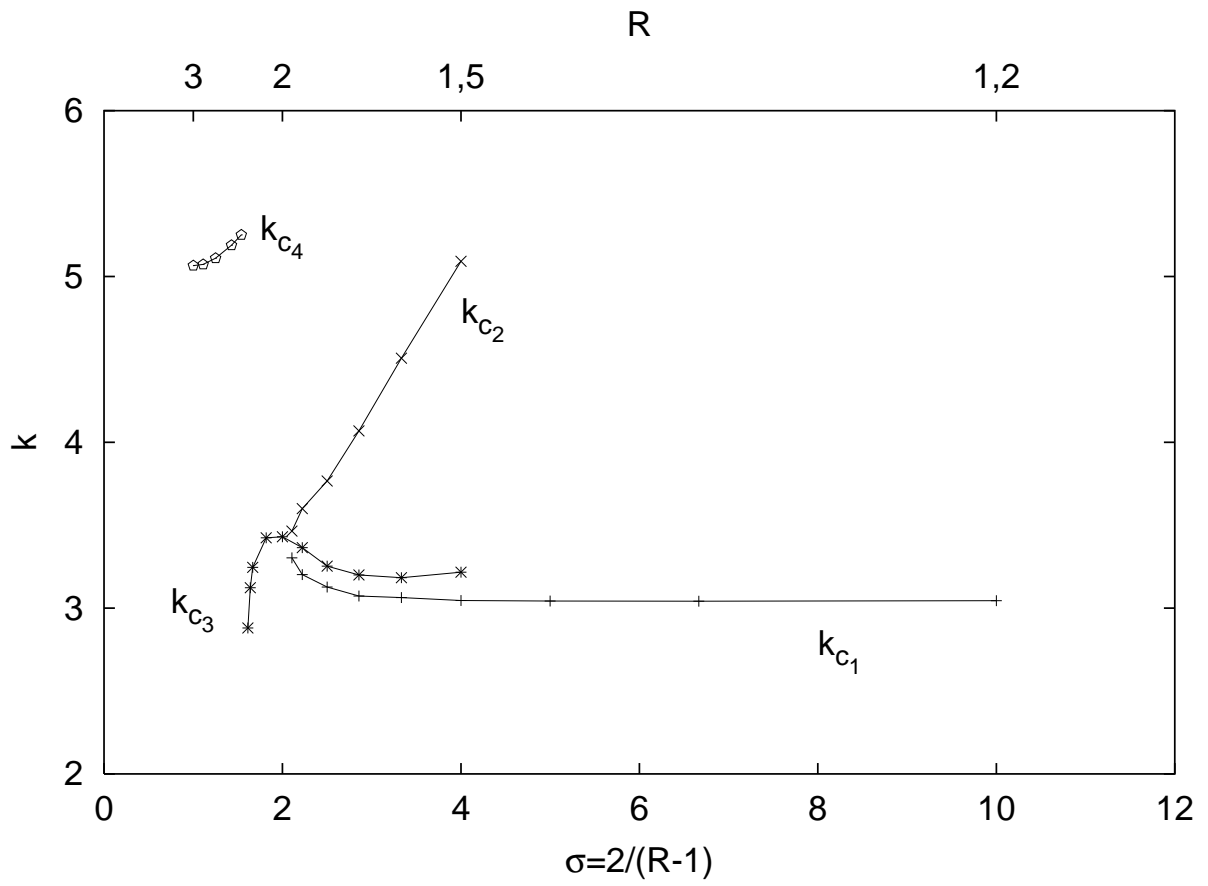


Figure 13: Giuseppe Petrone, Physics of Fluids

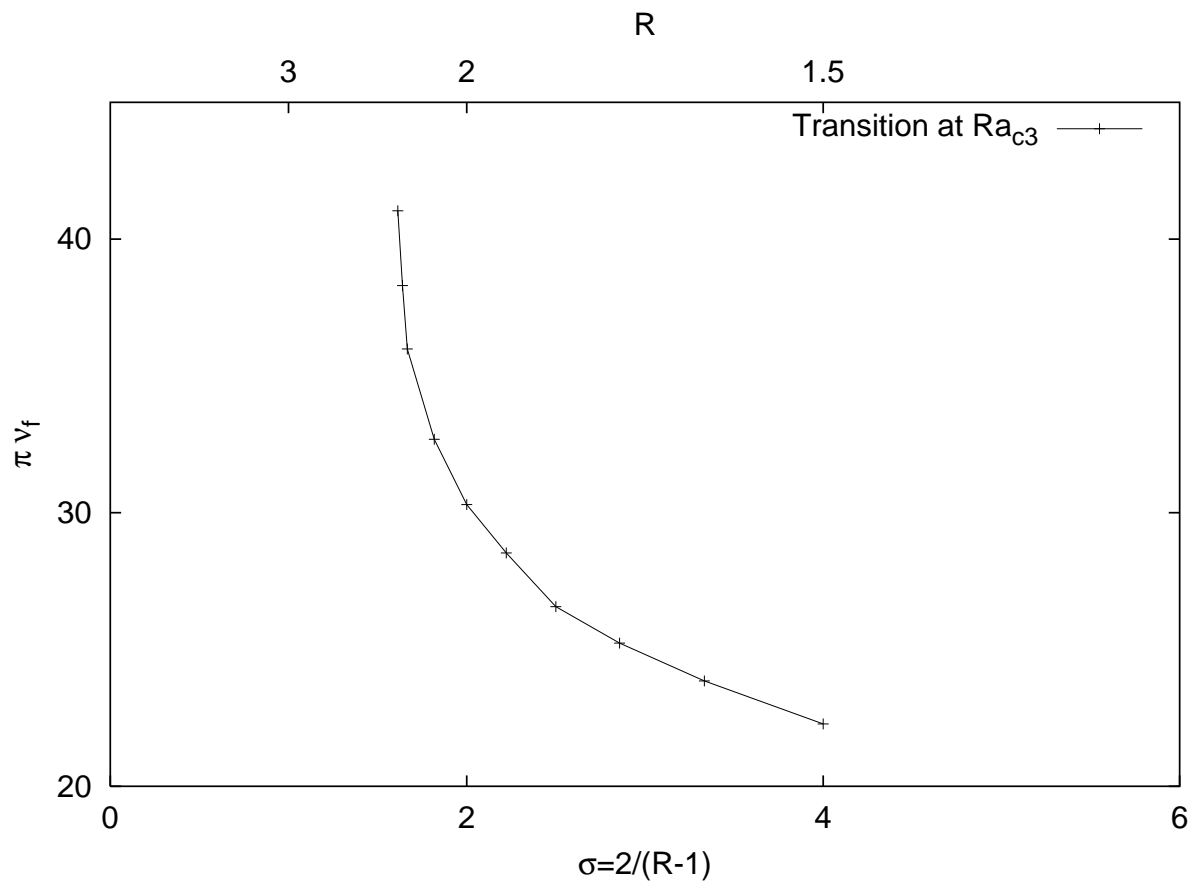


Figure 14: Giuseppe Petrone, Physics of Fluids

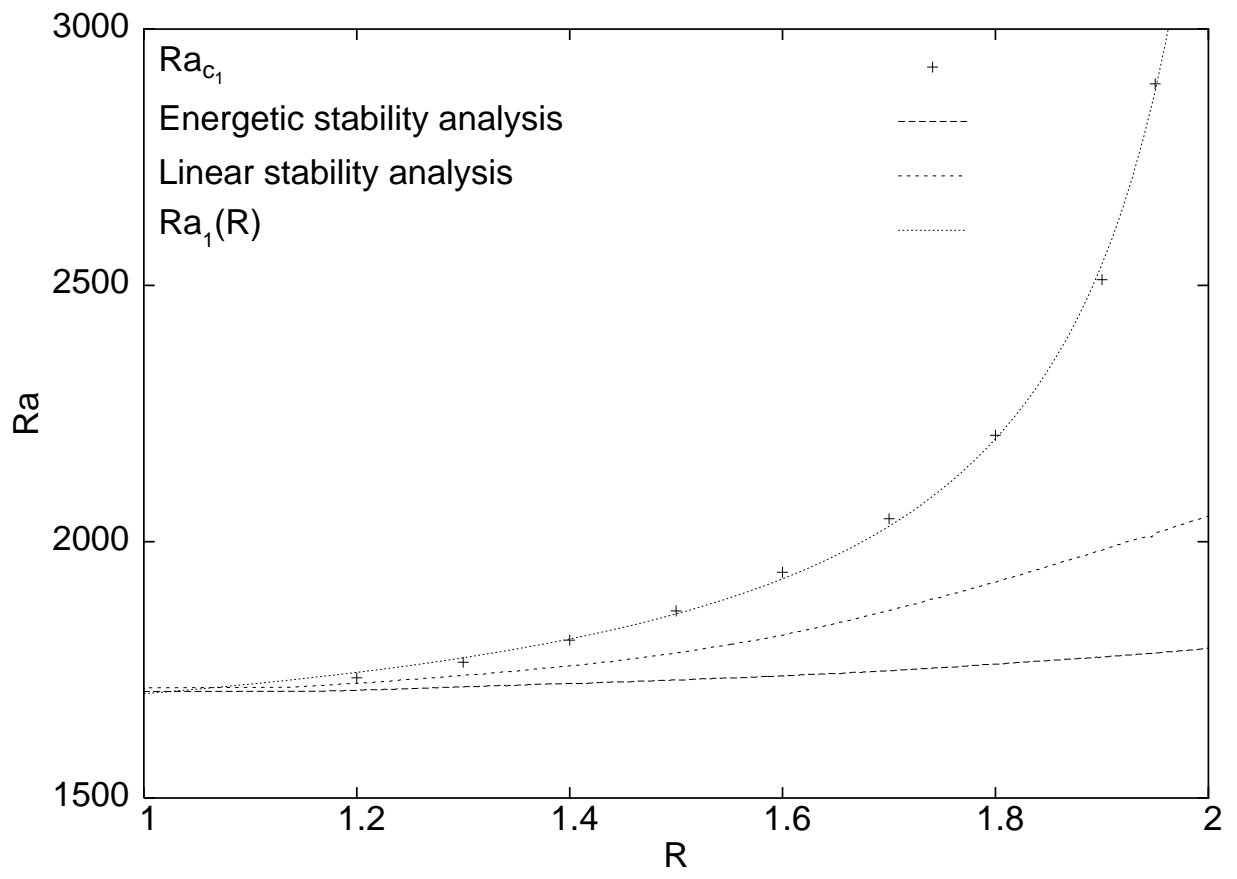


Figure 15: Giuseppe Petrone, Physics of Fluids